U.PORTO

FEUP **FACULDADE DE ENGENHARIA**
UNIVERSIDADE DO PORTO

M 2019

EFFECT OF HEAT TREATMENT ON SLM MARAGING C-300 STEEL PARTS

ABEL LOUREIRO OLIVEIRA
DISSERTAÇÃO DE MESTRADO APRESENTADA
À FACULDADE DE ENGENHARIA DA UNIVERSIDADE DO PORTO EM ENGENHARIA METALURGICA E DE MATERIAIS

ORIENTADOR
Professor Doutor Manuel Fernando Gonçalves Vieira

Candidato	Abel Loureiro Oliveira		*Código*	200502152
Título	Effect of heat treatment on SLM Maraging C-300 steel parts			
Data	03 de setembro de 2019			
Local	Faculdade de Engenharia da Universidade do Porto – Sala F106 - 11:30h			
Júri	*Presidente*	Laura Maria Melo Ribeiro		DEMM/FEUP
	Arguente	Fernando Jorge Lino Alves		DEM/FEUP
	Orientador	Manuel Fernando Gonçalves Vieira		DEMM/FEUP

Abstract

This dissertation has been executed as part of a broader investigation on Additive Manufacturing of components for the automotive industry, for the conclusion of the master's degree in Metallurgical and Materials Engineering at the Faculty of Engineering of the University of Porto. The purpose of this work has been to evaluate the response of Maraging C-300 steel parts produced by Laser Powder Bed Fusion Metal Additive Manufacturing to age hardening heat treatment requiring the least resources possible and to assess the quality of the structures produced.

Initially, this work introduces Additive Manufacturing and emphasizes the advantages of its implementation on an industrial environment and the particular challenges and limitations of Metal Additive Manufacturing, especially the reproducibility of parts and microstructures. Secondly, the processing issues of LPBF (SLM) are exposed highlighting the physical mechanisms that rule metal laser-fusion, the resulting structures and the structural defects, particularly those encountered in the parts under study. Thirdly, the materials and experimental procedures of this work are described, followed by the results obtained, which are then discussed.

The objective of this dissertation was to assess the structure of SLM processed components with a specific geometry, used in cable harness production for the automotive industry. These parts were then used to optimize the aging treatment conditions to maximize the mechanical response of SLM tensile test parts built in two different orientations.

The parts exhibited vertical surfaces with high roughness and a very thin microstructure with few process-induced pores and a considerable amount of Ti-Al oxides, likely due to an excess of oxygen in the melt. These parts were cut into small samples for test aging treatments and the highest hardness condition (6 hours at 490 ºC) was chosen for the aging heat treatment of the tensile test samples. The tensile test samples yielded mechanical resistance similar to conventionally fabricated parts, although with considerably less ductility. No significant anisotropy was measured between specimens built with the major axis perpendicular or parallel to the powder bed.

Key Words

Additive manufacturing; heat treatments; maraging steel; microstructural characterization; SLM.

Resumo

Este trabalho de dissertação em engenharia metalúrgica e de materiais é parte de um projeto de investigação mais vasto sobre fabrico aditivo de componentes para a indústria automóvel. O principal objetivo foi avaliar a resposta de componentes em aço Maraging C-300, produzidos por fabrico aditivo, a tratamentos térmicos de envelhecimento. Com estes tratamentos procurou-se minimizar o tempo e temperaturas exigidos mantendo as propriedades dos componentes produzidos.

Este trabalho começa por introduzir o processamento de componentes metálicos por fabrico aditivo enfatizando as vantagens da sua implementação na indústria, mas também as suas limitações e desafios a superar, especialmente a reprodutibilidade de microestruturas e componentes. É também apresentado o processo de fabrico por laser em cama de pó (SLM), destacando os mecanismos físicos que controlam a fusão de metal por laser, as estruturas resultantes e os defeitos estruturais, particularmente os que foram encontrados nas peças analisadas.

Seguidamente, descrevem-se os materiais e o procedimento experimental e são apresentados e discutidos os resultados obtidos. Foi caracterizada a microestrutura de componentes usados no fabrico de cabos para a indústria automóvel; desses componentes foram cortadas amostras para o teste das condições de tratamento térmico de envelhecimento a serem aplicadas a provetes de tração, os quais foram produzidos em duas direções diferentes e solicitados à tração.

As superfícies verticais dos componentes exibiam uma maior rugosidade, tendo sido observada alguma porosidade e a presença de óxidos de Ti-Al, provavelmente devido a um excesso de oxigénio no banho. Os componentes foram cortados em pequenas amostras que foram submetidas a tratamento térmico. As condições associadas a maior dureza (6 horas a 490ºC) foram selecionadas para tratar os provetes de tração que apresentaram uma resistência mecânica semelhante à de materiais produzidos por processos convencionais, mas com menor ductilidade. Os provetes de tração construídos com o eixo de solicitação mecânica perpendicularmente à cama de pó apresentaram resultados semelhantes aos produzidos com esse eixo paralelo à cama de pó.

Palavras-Chave

Acknowledgements

Above all, I would like to express my deepest gratitude to Professor Doutor Manuel Fernando Gonçalves Vieira for literally everything.

I would also like to express my gratitude to Professora Doutora Laura Maria Melo Ribeiro, Doutor Omid Emadinia, Professora Doutora Filomena Maria da Conceição Viana, Professora Doutora Sónia Luísa dos Santos Simões and Sr. José Ramiro de Sousa Soares.

Table of Contents

List of Figures

List of Tables

Acronyms and Symbols

Acronyms	Description
3D	Three-dimensional
AM	Additive Manufacturing
APT	Atom Probe Tomography
ASTM	American Society for Testing and Materials
CAD	Computer-aided Design
CNC	Computer Numerically Controlled
DED	Direct Energy Deposition
DEM	Department of Mechanical Engineering
DEMM	Department of Metallurgical and Materials Engineering
DMLS	Direct Metal Laser Sintering
E	Energy Density
EB	Electron Beam
EBSD	Electron Backscatter Diffraction
EDS	Energy-dispersive X-ray Spectroscopy
EPBF	Electron Beam Powder Bed Fusion
FEUP	Faculdade de Engenharia da Universidade do Porto
G	Temperature Gradient
GMA	Gas Metal Arc
HRC	Rockwell C Hardness
HV	Vickers Hardness
L	Laser
MAM	Metal Additive Manufacturing
ME	Marangoni Effect
MP	Melt Pool
MPB	Melt Pool Boundaries
MPS	Melt Pool Shape
MS	Maraging C-300 Steel
PA	Plasma Arc
PBF	Powder Bed Fusion
R	Solidification Growth Rate
RP	Rapid Prototyping
RP	Recoil Pressure
SDAS	Secondary Dendrite Arm Spacing
SEM	Scanning Electron Microscopy
SLM	Selective Laser Melting
SR	Surface Roughness
SRμT	Synchrotron Radiation micro-Tomography
SS	Stainless Steel
STL	Standard Tessellation Language
TMG	Thermal Gradient Mechanism

1 Introduction

Additive manufacturing (AM) encompasses several bottom-up manufacturing technologies that print finished or intermediate parts layer by layer, from a digital 3D model, through deposition, melting or sintering, and consolidation of the physical slices that constitute the part. Processing requires little or no process planning and understanding of the AM equipment and materials used. AM technologies can potentiate and convey the advantages of rapid prototyping, from which it evolved, to the fabrication of final products and have the potential to shift the manufacturing paradigm of localized and concentrated mass production in large factories, with dedicated tooling and high costs, to a mass customization and distributed manufacture concept, with parts available on demand, when and where they are needed [1].

AM processing has great inherent versatility, adaptability and customizability regarding design, geometry and material, almost without impacting cost. These technologies may be introduced anywhere in the product life cycle, from prototyping to full scale production, for tooling applications or post production repair. The process enables innovative structural design, allowing for the manufacture of highly complex and otherwise unfeasible shapes. Regardless of complexity, building is generally performed in a single step and complexity does not implicate added cost [1].

AM is yet to fulfil its potential. The main challenges encompass: design; process modelling, simulation and control; materials; processes and machines; qualification and certification. Metal AM (MAM) presents particular challenges mainly due to the specific solidification conditions and thermal processing cycles entailed, thus requiring a better understanding of the complex relationship between processing, microstructure and properties. Process repeatability and part reproducibility across machines and materials is a major issue to be overcome if MAM is to become a widespread implemented technology. AM still requires optimization of building parameters for a specific part geometry or type of material, the orientation and even the layout of the parts within the building area may induce variance [1-4].

This work aims at assessing the structure and mechanical performance of parts produced in maraging C-300 steel (MS) by SLM (EOS´s MS1 powder processed by DMLS in an EOS

M290), through hardness, tensile and shock testing, as well as the optimization of the heat treatment for the maximization of mechanical properties.

1.1 MAM Technologies

According to the ASTM F2792-12a standard [5] the categorization of direct MAM technologies firstly separates powder bed fusion (PBF) from direct energy dispersion processing (DED). The type of primary heat source provides further distinction within both categories, namely: laser (L), electron beam (EB), plasma arc (PA), and gas metal arc (GMA). PBF systems are either equipped with a laser (LPBF), henceforth referred to as selective laser melting (SLM), of which DMLS (Direct Metal Laser Sintering) is EOS's trade mark variant, or with an electron beam (EPBF), operating in high vacuum. DED resorts to any of the mentioned heat sources, further distinction lies on the feedstock. DED systems may use powder (powder-feed systems) or wire (wire-feed systems) delivered through nozzles in the moving heat source-feeding integrated head; these processes integrate a multi-axis control system for precise relative movement of the build and the heat source. PBF and DED are direct-to-metal processes that produce parts requiring a minimum of post-processing steps (heat treatment, finishing), but DED is often used to produce large "blank" shapes requiring extensive machining to achieve the intended final geometry.

1.2 The SLM Process

AM processing starts with a comprehensive 3D digital representation of the geometry of the part generated through CAD software modelling or laser-scanning of an existing part. The CAD file is converted to a STL file describing the external closed surfaces of the CAD model, which is the basis for the calculation of the slices. The STL file is transferred to the AM machine and the scale, layout, position and orientation of the parts is set by the operator. Machine manufacturers provide standard/default setups for each material developed and provided by them, with optimized settings that prioritize processing speed or surface finish and detail or a compromise parametrization. The build is a completely automated sequence of layer deposition, selective fusion and consolidation [1].

The process occurs inside a chamber filled with inert gas (see Figure 1). Temperature is typically kept around 200ºC and the substrate may also be heated. The building platform is lowered corresponding to the layer thickness so that the first powder layer may be

spread across the build area using a counter-rotating powder levelling roller or a rake. The spreading mechanism overshoots the building platform to dump any excess powder into a recovery vat. The laser beam impinges on the powder bed, directed by galvanometers, thereby tracing the scanning pattern and selectively melting the material to form the first slice. Surrounding powder remains loose and serves as support for subsequent powder layers. After melting and consolidation of each layer, the build platform is again lowered by one-layer thickness and a new layer of powder is laid so that the laser may draw the subsequent slice. This process repeats until all layers, which incorporate any support structures, are formed and the complete part is built. A cool-down period is typically required to allow the parts to uniformly cool to an appropriate temperature for handling and exposure to ambient temperature and atmosphere. Post-processing requires the cleaning of excess powder and removal of the substrate and support structures. The final application of the produced parts may require consolidation, finishing, heat treatment, coating or assembly operations [1].
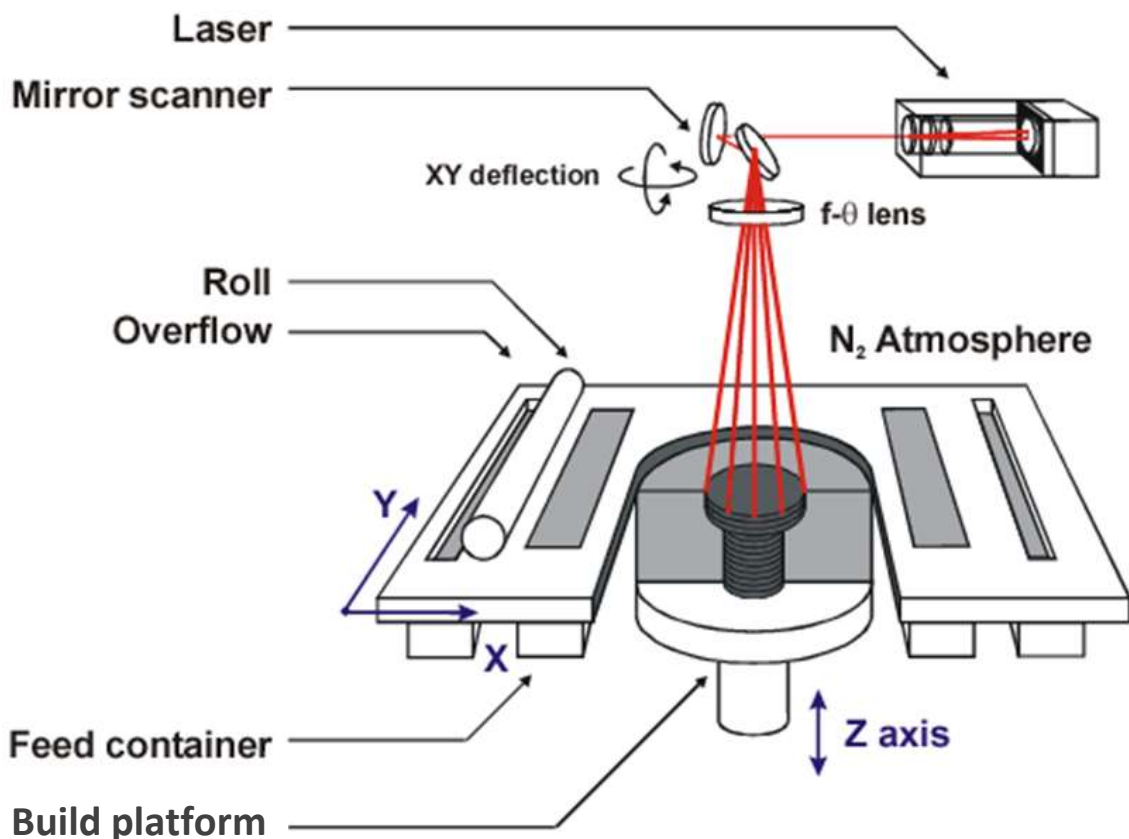
Figure 1: The SLM process apparatus.

1.3 Maraging C-300 Steels

Maraging C-300 (or 18Ni-300) steel is part of the class of ultra-high-strength steels (>1000 MPa). MS are distinctive by combining high strength with relatively good ductility, good hardenability and weldability, requiring a simple aging heat treatment. This properties assortment is of great importance in automotive, nuclear, gear, bearing and especially aerospace and tooling industries. Materials combining these properties with the geometrical optimization granted by AM, which partially compensates for the relatively high density of iron alloys, are key to the future development of lightweight engineering design strategies.

MS are Fe-Ni-Co-Mo-Ti alloys exhibiting a low carbon Fe-Ni lath martensite (bct) matrix, hardened by precipitation, during ageing, of finely dispersed (~100 nm apart) Ni_3Ti and Fe_7Mo_6 nanoscale (5-20 nm) intermetallic phases at around 500 °C. None of the hardening mechanisms involve carbon, neither through carbide precipitation nor solution hardening. The typical thermal processing of MS involves the solution annealing of as-fabricated parts at 850°C for 1h to recover and homogenize the austenitic (fcc) matrix, and subsequent air cooling to room temperature for a complete martensitic transformation (Ms 200-300 °C) by a diffusion-less shear reaction, followed by aging between 480-510 °C for 3-8 hours. Overaging leads to austenite reversion and retained-austenite growth [6-8].

2 SLM Processing

MAM presents demanding requirements, such as energy densities suited for melting metals well over 1500°C, high thermal conductivity, propensity to oxidize, high surface tension, and lower absorptivity. These requirements make metals significantly more difficult to process than polymers, as heat shielding, insulation, temperature and atmospheric control are much more stringent. MAM requires a platform onto which the first layer of supports may adhere and consolidate, becoming part of the build. Power requirements from the heat source and the handling of higher density materials, as steels, are also greater. Figure 2 attempts to illustrate the complex interaction between the numerous processing factors implicated in powder MAM. Main inputs encompass: the equipment, part's geometry, build chamber conditions, scanning parametrization and materials. The thermal interactions ensuing heat input include: heat source-material interaction, heat and mass transfer and

flow, processing temperature and thermal history. The outputs are the parts produced and hopefully the consequent conformity of geometry and properties to the targeted specifications [1, 9].
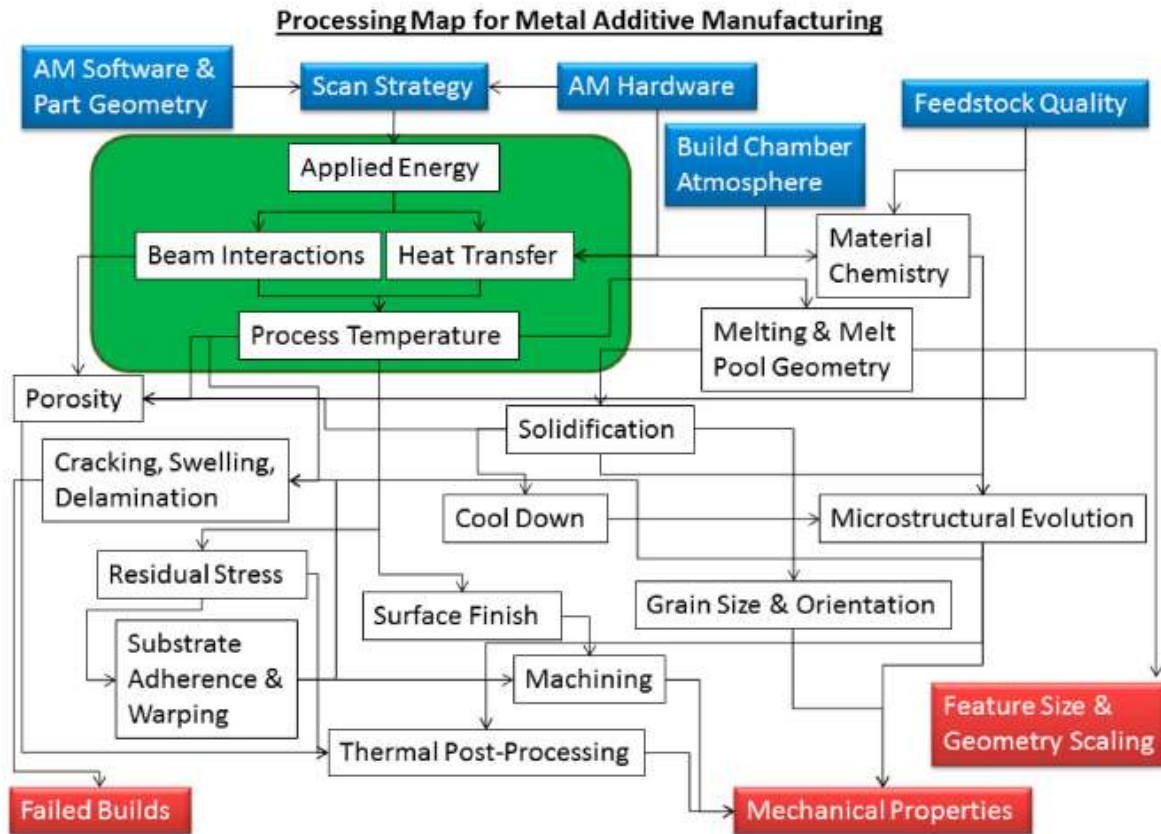
Figure 2: Relationship between processing parameters in MAM [9].

2.1 Building Chamber Atmosphere

The atmosphere in which the metal is processed influences chemistry, heat transfer, processability and defect generation. Most metal powders oxidize and retain humidity, while exposure to air and high temperatures can drastically increase the rate of oxidation; heat concentration may lead to localized oxidation of the finer details. SLM processing is conducted in an inert atmosphere of N_2 [10-14] or Ar [15], filling the chamber. N_2 can be incorporated into the part and reduce the fraction of martensite through its stabilizing effect on austenite [16]. The M290 equipment can operate with both atmospheres; the MS1 powder used for this work is processed in N_2 [17].

2.2 Powder

The quality of the powders used is essential to the quality of resulting MAM parts and is determined by the size and size distribution of the particles, their shape, surface morphology, chemical composition, homogeneity, and internal porosity. Most of these features will influence the ability of the powder to flow (flowability) and to densely pack (apparent density), which are essential parameters (ASTM B213-13 and B212-13 standards, respectively) since these greatly affect processability [18, 19]. Both are improved by spherical particles while rough particle surfaces and satellites are detrimental; although finer particles hinder flowability, they typically increase apparent density by filling the interstices between larger particles [20, 21].

Powder characteristics are mostly consequence of the atomization technic used to produce them, all of which yield more of the relatively larger particles, thus increasing the cost of the finer powders. Gas Atomization is the most common in SLM of MS [10-15] with a typical particle size distribution having a D_{50} below 45 μm. EOS claims a maximum particle size below 63 μm for 95 wt% of MS1 powder. Gas Atomization provides particles with satellites and with pores, from gas incorporation during production, which is released during SLM, possibly causing powder-induced porosity. Plasma Rotating Electrode yields highly spherical and smooth particles without porosity [22].

Liu *et al*. [23] tested the effect of varying size distribution of 316L powders with similar mean sizes (D_{50} ±28μm). A wider range of particle size, containing more fine particles (<10μm), provided a higher density of parts (>99%) and smoother side surfaces across a wider range of parameters (spot size, speed) than a narrower size range, which provided better flowability. Spierings *et al*. [24] reports that smaller 316L powders (D_{50} of 15 μm and 28 μm) require a lower energy density to achieve 99.5% density than larger powders (D_{50} of 38 μm) and that the former promote surface quality and mechanical strength while the latter allow for higher elongations.

2.3 Surface Roughness and Feature Size

The minimum feature size is determined by the minimum focused spot size achievable by the beam, which is proportional to its wavelength, and by the powder size. SLM technologies provide the best resolution and finish within MAM with a typical layer

thickness between 20-50 μm and spot sizes of 75-100 μm. EOS claims an accuracy of about 50 μm and 0.1 % for small/optimized and larger/intricate parts, respectively, and a minimum wall thickness of 0.3-0.4 mm with EOS's MS1-performance default parameter set (layer thickness of 40 μm). As-built top-horizontal and vertical surface roughness values, Ra and Rz, of 5 μm and 28μm, and of 9 μm and 50 μm, are reported for the 40 μm and 50 μm (MS1-speed) layer thickness parameter sets, respectively. R_z values <0.5 μm are achievable after polishing [17].

Surface roughness (SR) depends on several interlinked strictures namely: powder, process and parametrization, part design and post processing; these result in two main sources of SR. One is determined by the layered nature of the process, which attempts to approximate curved or inclined surfaces with a curved stair-step delineation; the average SR will strongly depend on the layer thickness and on the orientation of the surface relative to building direction [9, 14, 17]. Secondly, SLM is prone to satellite adhesion due to the sintering of powder particles onto parts' surfaces [9, 14] or melt ball formation by the balling phenomenon [25, 26]. Typically, SR is lowest in top horizontal surfaces, especially if re-melted, and higher elsewhere from the stepped profile and MP interaction with loose alongside powder; however, high speed scanning may induce unstable melt flow and met splashing, which can cause porosity, thus increasing SR on top surfaces [27].

The first can be mitigated by reducing the layer thickness [9, 27] entailing more layers to produce a part, thus considerably more time; alternatively, it may be possible to orientate the build to avoid wide angles between parts' surfaces and build direction [28]. The other arises from coarser feedstock and inadequate heat input, causing MP instability and spatter [25, 26]. Partially melted particles stick to the surfaces of the part and the resulting average roughness is in the order of magnitude of the mean powder size [26]. High scanning speeds elongate the MP, thereby promoting Raleigh instability, which can generate track necking and beads of molten metal (balling); these are dragged to the side edges of the track by the surface tension gradient driven flow inside the MP. Balling can be completely avoided through optimization of laser power and speed parameters [26].

2.4 Laser-Powder Interaction

2.4.1 Laser

Together with high-speed low-inertia mirror galvanometers, lasers are fast and agile high-power density heat sources, providing a continuous or pulsed beam whose spot size, shape and energy density profile can be modulated in real time. To yield fully consolidated (>99.9 %) steel parts the lasers equipping SLM systems had to evolve from the CO_2-gas lasers ($\lambda \approx 10.6$ μm), adapted from the SLS process, to diode pump Nd:YAG-crystal lasers ($\lambda \approx 1.064$ μm). Modern SLM systems resort to more compact, robust and highly efficient diode pump Yb:YAG-fiber lasers ($\lambda \approx 1.030$-1.070 μm) of 200-400 W [29]. The M290 uses a 400 W Yb-fiber laser and F-theta lens capable of scan speeds up to 7 ms^{-1} and a focus diameter of 100 μm.

2.4.2 Absorptivity

The laser provides a coherent and collimated stream of monochromatic photons whose energy transfer to the material is mainly dependent on the material's absorptivity to a given radiation. This quantifies the fraction of impinging energy effectively absorbed and, consequently, the efficiency of incident radiation conversion into heat through electron excitation and subsequent kinetic energy transfer to the lattice.

The absorptivity depends mainly on material's chemistry, temperature and surface state (oxide layer, roughness/topography, contaminants and defects), beam's intensity/speed, spot size and energy density distribution profile, and wavelength. Raising laser power to compensate for low absorptivity would lead to spatter ejection and porosity [30].

When a photon hits a particle, part of the energy is absorbed while the rest is reflected, thereafter undergoing multiple reflections until it emerges outside of the powder bed or its intensity becomes negligible. The powder bed is an open-pore reflective structure that enhances absorptivity through multiple reflections between particles, whereby radiation can penetrate deeper than the mean particle diameter [31]. The absorptivity of 316L (λ=1 μm), at room temperature, increases from 0.34, on a flat surface, to 0.68, and is relatively insensitive to powder arrangement structure [32]. The absorptivity of powder blends depends on that of its components and their volume fraction; high alloy steels approach 0.8 (λ=1 μm) [33]. Furthermore, for metal powders, shorter radiation wavelengths allow

higher absorptivity [33, 34]. The absorptivity of loose iron powder increases from 0.45 to 0.64 when exposed to CO_2 ($\lambda \approx 10.6$ µm) or Nd:YAG ($\lambda \approx 1.064$ µm) radiation, respectively [31, 33].

2.4.3 Heat and Mass Transfer and Fluid Flow

SLM is a heat driven process whose temperature and velocity distributions and cooling rates must be measured and understood. This requires precise knowledge of highly dynamic and fast evolving transient temperature fields, which are localized and reach metal boiling temperatures. These fields are generated by a fast-moving heat source and evolve at the bulk scale within a variable geometry. This heat evolution is very hard to monitor, and precision is critical, since mass transfer and fluid flow mechanisms often have an exponential correlation to temperature. However, experimental methods are costly and time inefficient. Furthermore, data provided by thermocouples and infrared thermography is very limited. Therefore, the development of computation models and predictive simulations properly validated by experimental temperature vs time data are crucial to further understand MAM.

The heat source characteristics and parametrization, together with material properties, control heat absorption, inducing huge temperature gradients, which shape the melt pool (MP), thereby vastly determining the solidification kinetics (section 2.7).

Due to the high scan speeds, the isothermal profiles generated by the laser are elongated in the wake and compressed in front of the beam (Figure 3). The difference in thermal properties between materials generates large differences in the heat affected zone and melt pool shape (MPS) for a given process parametrization [35].

2.4.3.1 Surface Tension, Marangoni Effect and Recoil Pressure

Khairallah *et al*. [36]. developed a high-fidelity mesoscopic model to simulate the physical mechanisms in LPBF processing of 316L, using a laser ray tracing heat source (200W at 1.5 ms^{-1}) that models contact point/area heat transfer, including particle shadowing and partial melting. It simulates 3D fluid flow due to recoil pressure (RP), the Marangoni effect (ME), and evaporative and radiative surface cooling. Figures 4a-c illustrate the impact of temperature dependent physics on MP characteristics.
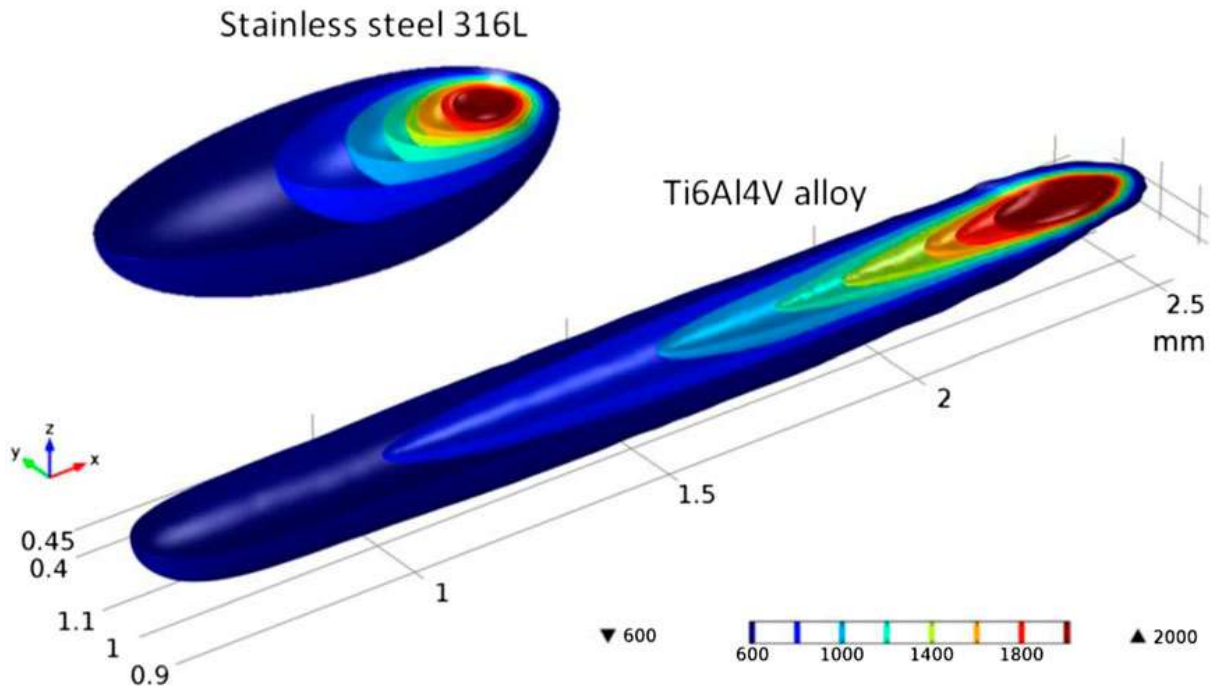
Figure 3: Isosurface temperature contours during laser scanning of 316L SS and Ti6Al4V alloy [35].
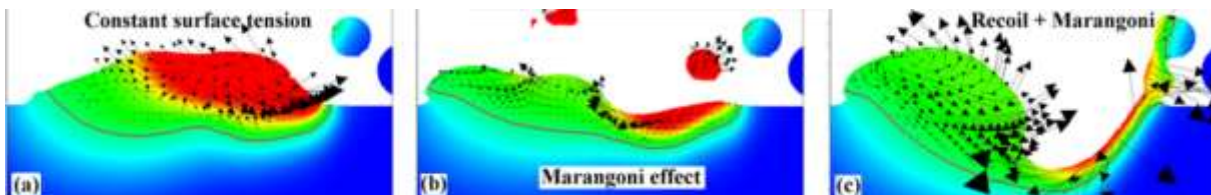
Figure 4: Effect on MPS and flow of (a) constant surface tension, (b) temperature dependent surface tension and (c) recoil pressure [36].

Temperature dependent surface tension (ST) enables the simulation of the ME, which drives melt flow, hence enabling convection cooling and low viscosity spattering. The temperature inside the MP is greatest near the beam axis and lowest near the MP boundaries. This temperature gradient generates a spatial gradient of interfacial tension (surface tension gradient), which creates the Marangoni shear stress on the top surface of the MP that drives the recirculating flow of metal inside the MP. The convective flow redistributes heat within the MP, whose circulation pattern greatly impacts the temperature distribution within the liquid, thus affecting the heating and cooling rates, which are determinant for the evolution of the solidification structure [9, 36, 37].

Melt composition also influences MPS. The surface tension of metals and alloys depends on temperature and composition, especially the concentration of surface-active elements like S, O and N in steels. In the absence of such elements the temperature coefficient of

surface tension is negative, generating a radially outward convective flow, resulting in wide, shallow MP. However, close to boiling point or under higher concentration of such elements, this convective flow is reversed, and the MP becomes deeper and narrower [37].

The recoil momentum pressure generated by the vaporization of the metal is proportional to the saturated vapor pressure; it can be simulated by Anisimov´s model [38] and is exponentially dependent on temperature. Below the laser spot, the temperature easily reaches boiling point, generating a vapor recoil pressure that shapes the MP surface into a topological depression. The combination of ME and RP greatly increases MP depth, hence MP surface area, leading to enhanced evaporative cooling. MP depth is sensitive to absorptivity whereas MP width depends mostly on spot size and shape [36, 37, 39].

SLM typically uses lasers with axisymmetric Gaussian power density distribution profiles and spot sizes of 100 μm. Roehling *et al*. [39] studied the effect of modulating the laser profile ellipticity for different equivalent spot sizes (100-175-250 μm) and power/speed combinations on 316L samples (Figure 5). Both, spot ellipticity and size, influence melt track configuration, MPS and laser heating mode (conduction or keyhole). More importantly, whilst in conduction mode, elliptical profiles allowed direct and localized real-time microstructural control between columnar, equiaxed or mixed microstructures across a wide power/speed range.

2.4.3.2 Scan Track and Melt Pool Shape and Strong Mass Flow

MPS and flow vary with material thermal properties and composition, topological features, laser intensity/speed, spot size, shape, energy distribution and focal point height [30, 35-37, 39]. Considering the exponential dominance of RP at the depression and the prevalence of ST driven flow at cooler areas, the MP (in quasi-steady-state) forms three zones: the depression below the beam, the tail end, and a transition zone in-between (Figure 6 shows 500 μm along laser path at 241 μs). The depression acts as a source of liquid, feeding the transition zone, which displays a net backward flow. As the track gets longer and cooler this flow starts to break, thus defining a distinctive tail section of non-uniform flow. Track necking is reminiscent of the Plateau-Rayleigh instability, from ST and wetting conditions, but also influenced by local interactions of the liquid with particles alongside the track through partial melting and denudation zones.
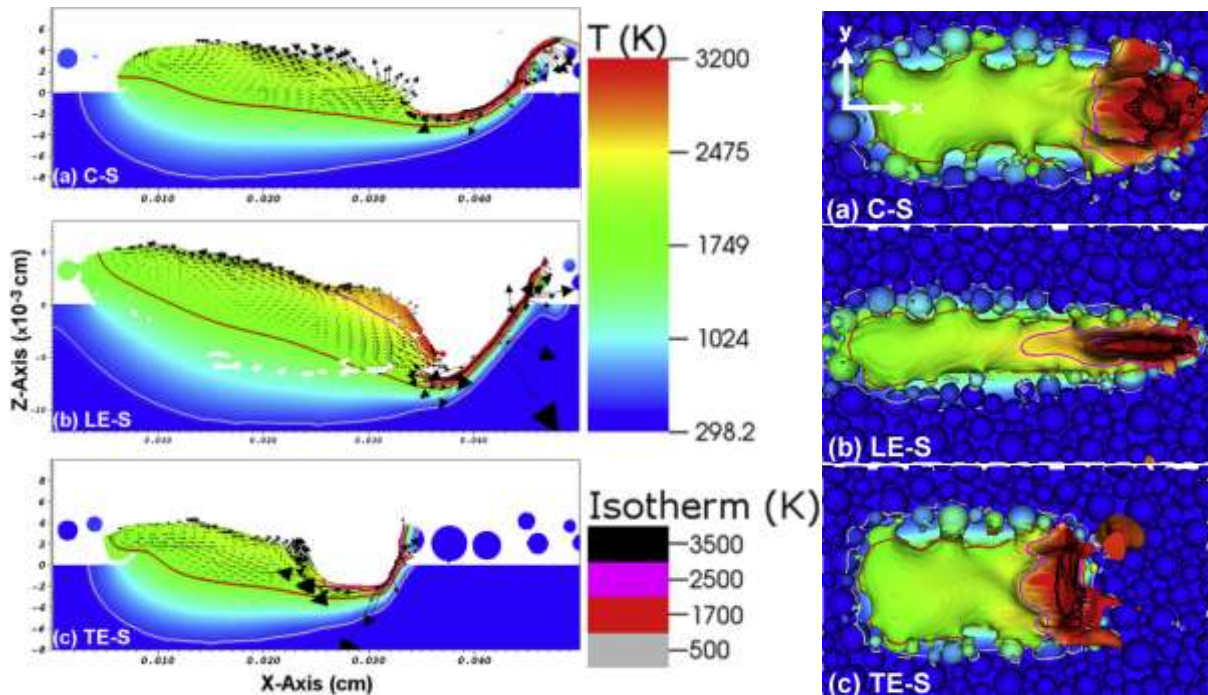
Figure 5: Side-view (left a to c images) and top-view (right a to c images) of Gaussian (a), longitudinal elliptic (b) and transverse elliptic (c) laser spot configuration induced melt pool shape [39].
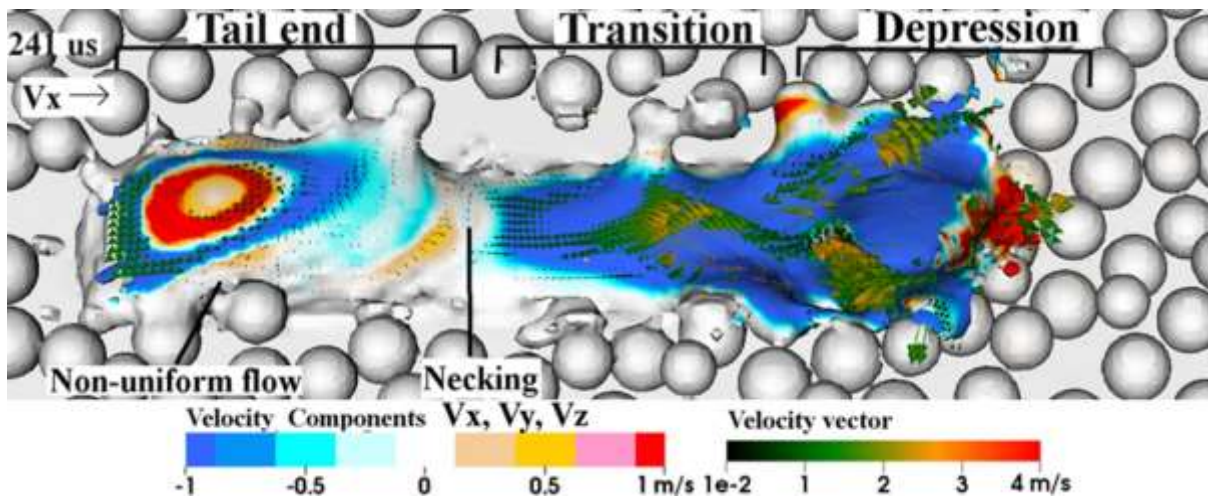
Figure 6: Melt pool flow at quasi-steady-state [36].

Under the laser spot (Figure 7a at 76 µs), RP becomes dominant, inducing a strong dynamical flow and creating a topological depression. The pressure exerted against the inner walls of the cavity squeezes the liquid, which is radially accelerated (>4 ms^{-1}), leaving a thin liquid bottom layer where temperatures are highest (3500 K) [36].
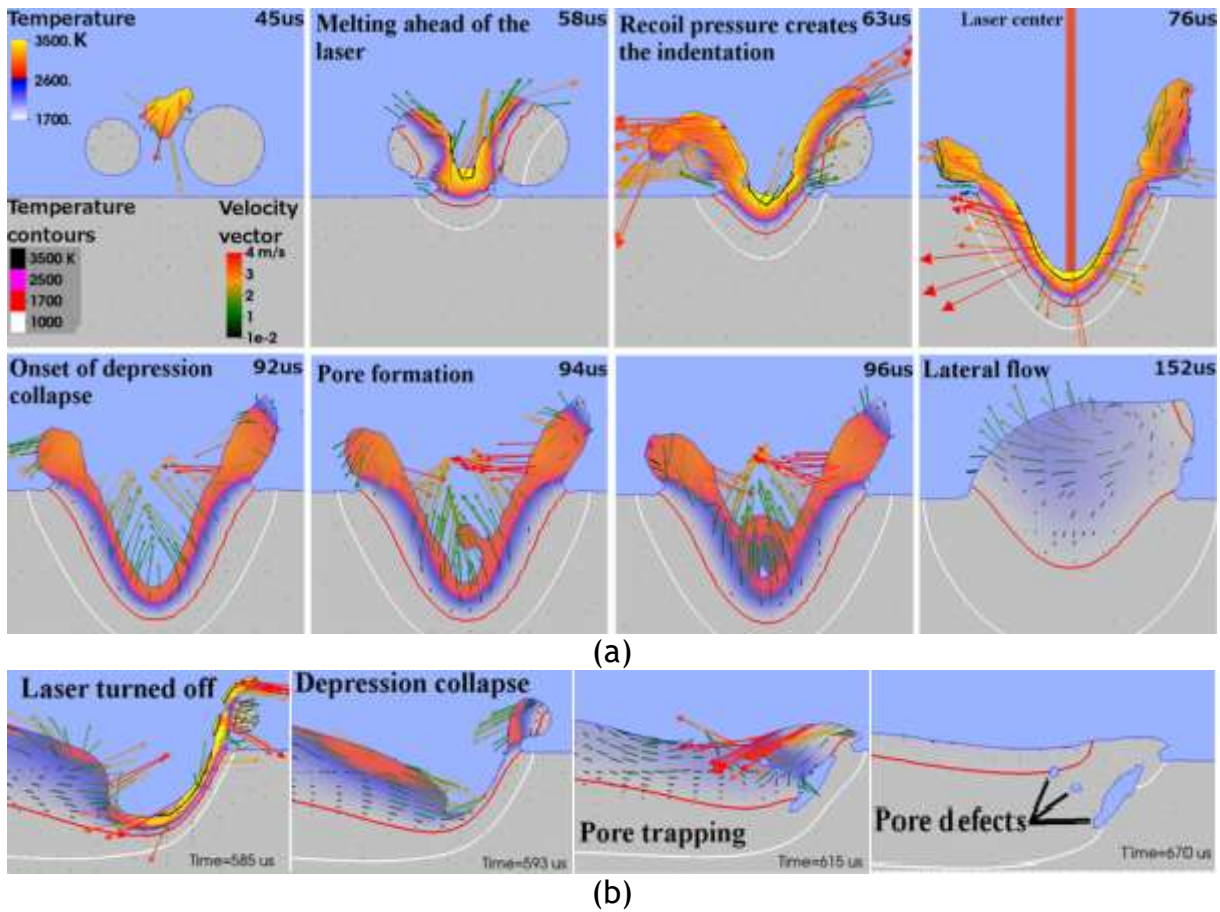
Figure 7: (a) Transverse slices of the track, from 58 to 152 μs, at fixed location, showing the temperature and velocity field of the melt as the laser scans towards the observer; (b) longitudinal slices of the melt track after laser shut down and subsequent pore formation (585 to 670 μs) [36].

Ahead of the laser (Figure 7a at 45-63 μs), the beam starts melting particles and indenting the substrate. Immediately ahead, the velocity vectors pointing away from the cavity's rim are greatest (>4 m/s), displacing the liquid up along the front/side walls where it accumulates, creating spatter and forward flow with enough momentum to displace particles ahead of the laser [36].

Behind the laser (Figure 7a >76 μs), temperature decreases fast and RP is superseded by ST. As pressure recedes the centrifugal flow vectors within the cavity become centripetal (Figure 7a at 92 μs), reversing melt flow inwards, causing its collapse. The strong flow, which can form vortexes following the laser and sudden flow inversion, especially with abrupt laser shutdown, increase the chance of trapping gas bubbles, possibly forming pores if captured by the solidification front (Figure 7b) [36].

Single-track scanning does not account for the flow asymmetries of a MP with randomly arranged passivated spherical particles on one side and a clean, smooth and more heat conductive surface available for epitaxial growth on the other; still, partial melting with surrounding particles can induce lateral flow (Figure 7a at 152 µs).

2.5 Process Parameters

The main machine parameters tuned for optimized SLM processing are: laser power P (Js^{-1}), speed V (ms^{-1}), spot diameter d (m), hatch spacing h (m), laser scanning pattern (or scan strategy) and layer thickness t (m). Process settings must be such that complete fusion of the particles and enough heat penetration to partially melt the underlying and adjacent solidified material is achieved, so that inter-particle, inter-track and inter-layer fusion and coalescence is accomplished.

Hatch spacing is the distance between adjacent tracks and is dependent on laser spot energy density distribution. If set too wide, solidification cracking [40], and aligned porosity between tracks [13, 41] can occur; if too low, leads to overheating [13]. Layer thickness is set per build and is limited by powder size. It greatly impacts building time. Excessive layer thickness leads to deficient inter-layer bonding, which, together with residual stresses, may cause distortion and inter-layer detachment (delamination) [9].

2.5.1 Power-speed relationship

Laser power determines the amount of photon energy per unit time irradiating the laser spot, while scan speed determines the duration of that exposure. The power-speed relationship is crucial, since only some combinations yield dense structures; these must fall within an experimentally determined parametrization window, which can be combined with G/R and GR data. Low energy density (low power-high speed) will result in insufficient melting, whereas high energy density (high power-low speed) will result in Keyhole laser operation mode, where MP depth is controlled by excessive metal evaporation and plasma formation; both cases lead to porosity. Conversely, in conduction mode the depth of the MP is controlled by heat conduction, the powder melts and the MP extends to the solid material beneath, thus welding both layers together.

Many researchers try to correlate different process parameters to define energy density indicators like specific energy, $E = P/Vd$ (Jm^{-2}) or volumetric energy density, $E = P/Vht$ (Jm^{-3}) or $E = P/Vdt$ (Jm^{-3}), which are arguably better predictors of parts relative density than power/speed combinations, but cannot avoid porosity or predict structure when power and speed attempt to compensate extreme values of each other to keep energy density constant [12, 16, 41, 42].

King *et al*. developed a predictive criterion for the conduction-to-keyhole transition threshold based on the linear dependence between MP depth and normalized enthalpy $\Delta H/h_s$ (specific enthalpy over enthalpy at melting), allowing the prediction of the combined effect of power, speed, and spot size (t=50 μm), across different materials [43].

2.5.2 Scan Strategy

Scan strategy refers to the path taken by the heat source over the powder bed to selectively melt each layer. The contour pass and the raster infill may be performed in continuous or pulsed laser modes. It may be set by build or by layer; the build plane, and consequently the orientation of the infill, is typically rotated by an angle and offset by 1 mm between each layer [9]. The DMLS Hatch Pattern starts with the contour pass performed with the laser spot shifted inwards by half its diameter (beam offset) [44]. The raster pattern may be done along x or y (Figure 8a and b), or both for a double exposure per layer (c); direction can be alternated between layers (d), or the scanning vector may be rotated by 67° between consecutive layers (e).
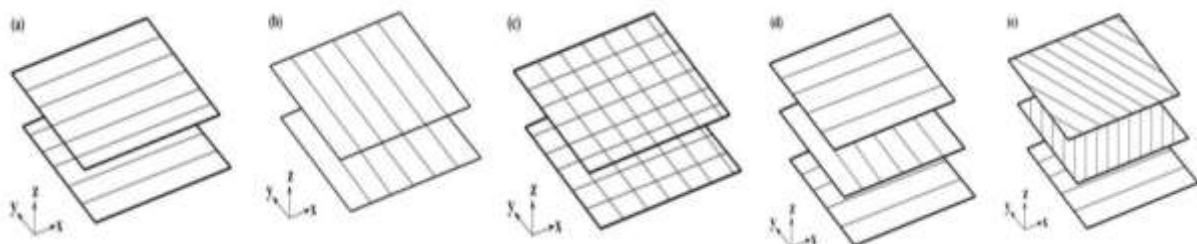
Figure 8: DMLS scanning patterns [44].

In the DMLS process, top surfaces, including up-facing slopes and curves, are designated *up-skin*, and are built in three layers, whereas downwards facing planes, inclined or curved surfaces, are designated *down-skin*, and built in two layers (see Figure 9). Different

parameters can be set for these areas, including power, speed and the overlapping between these zones and the core of the part to improve joining between them.

(a)   (b)
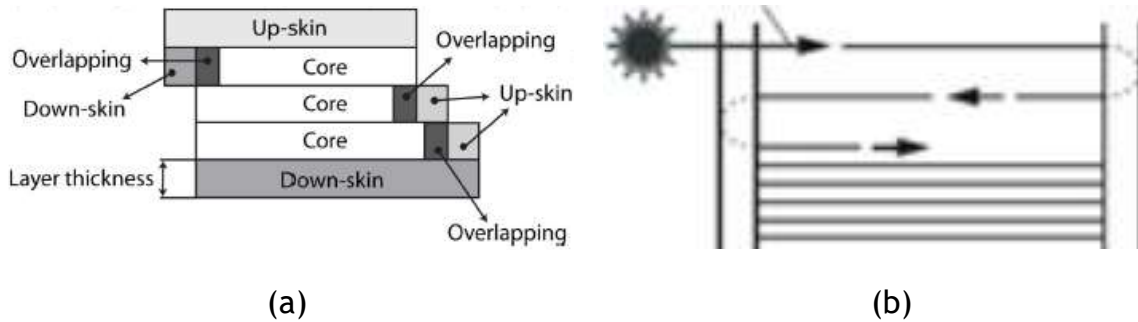
Figure 9: DMLS *up* and *down-skin* (a) and *sky-writing* (b) scanning procedures [44].

Mirrors have some inertia and require some time to accelerate. In DMLS processing, during bidirectional infilling, the laser will reverse direction at the edge of the scanning area, which would require a deceleration of the laser to accomplish the manoeuvre and subsequent overheat at the edges. To avoid this, as the raster vector reaches a contour, the laser is turned off while the mirrors continue as they decelerate to manoeuvre back and align with the next raster vector, where exposure resumes once the mirrors accelerate back and clear the contour. This technic is designated *skywriting* (Figure 9b).

2.5.3 Speed-Power Relationship and scan strategy

Heat flow within a build for a set speed-power combination varies significantly with scan strategy, part geometry and volume. Modelling has shown that poor powder thermal conductivity greatly influences MP size. As compared to solidified material, the powder acts as thermal insulator. Heat will flow significantly faster through the baseplate, or already consolidated material, hence, the edges, sloped or curved surfaces, overhangs or any features that maximize the local surface to volume ratio will be more prone to overheating. This is particularly detrimental to thin parts, since a thicker part will dissipate heat from the MP faster for a given speed-power combination. A contour pass prior to the infill of a layer will be considerably more thermally isolated by the surrounding powder and the beam may return to an edge without it yet having had time to dissipate the heat. Scan strategy should ensure that consolidated material has time, between passes, to cool enough as to avoid overheating; likewise, the infill with short scan vectors will result in sooner re-heating and partial re-melting of adjacent or underlying tracks.

Moreover, relative scanning direction between layers greatly impacts grain texture across layers and general residual stresses configuration. These factors imply that a power-speed criterion, even volumetric energy density, is over-simplistic, and not the best indicator of porosity formation due to local variations.

2.5.4 Maraging C-300 Steel SLM Processing Parameters

MS steel SLM processing parameters differ from system to system mainly because they must be optimized for maximum laser power. Optimal setup is frequently achieved empirically through experimental iteration, even if provided by the system supplier, to account for the specific geometry of a complex build.

A 100 W (Nd:YAG; 1.064 μm) laser allows a scan speed of 150 mm/s in continuous mode, with d between 1.8-2 mm, t of 30 μm and h of 0.62 d, to reach over 99 % density [10-12]. Reaching 99.4 % requires re-melting each layer by perpendicularly re-scanning each island at 150 mm/s, which doubles processing time; the increase of density to 99.48 % needs scanning at 100 mm/s with long scan vectors, which quadruples processing time, as compared to no re-melting. Finally, scanning and re-melting at 200mm/s, allows a 99.25 % density for a 50 % increase in time [10, 11].

A 200 W diode pumped Yb:YAG fibre laser in continuous wave mode with a d of 150 μm and a t of 30 μm enables speeds of 800 mm/s to reach 99.5 % (h 0.5-0.9d) and requires re-melting at 800 mm/s with h of 0.7 d to exceed 99.6 %. A double exposure at 600 mm/s and h of 0.7 d provided the highest density [13].

Casati's [15], Tan's [14] and Suryawanshi's [45] research groups claim fully dense parts. Casati *et al*. processed MS using a 200 W fibre laser with a 75 μm spot size; laser operation consisted of discrete 80 μs pulses, partially overlapping (point distance 65 μm), 80 μm hatch distance and 40 μm layer thickness. A meander scanning strategy with rotation of scanning direction of 67° was employed. Tan *et al*. processed MS1 powder in an EOS M290 with the following parameters: 370-400 W laser power, 40 μm layer thickness, 100 μm spot size; base plates were pre-heated to 40 °C; oxygen was kept under 0.6 vol% by continuously pumping N_2. Suryawanshi *et al*. [45] used a 180 W laser, 600 mm/s scanning speed, 30 μm layer thickness and 30 % hatch overlap.

2.6 Defects

2.6.1 Porosity

Porosity is always a concern in bottom-up building/consolidating processes, so it is transversal to AM technologies and can drastically impair mechanical properties. Macroscopic porosity, either between tracks or between layers, is due to insufficient heat penetration when hatch spacing (inter-track porosity), or layer thickness (inter-layer detachment) is too high. Generally, in MAM, microscopic porosity forms with two shapes: the round pore and the irregular pore. Round pores form by gas entrapment and are either high heat-input process-induced or powder-induced, while irregular pores are low heat-input process-induced, either from lack-of-fusion or shrinkage porosity due to an incomplete flow of metal to the solidifying region [9, 37].

Powder-induced porosity arises when gas incorporated by the powder particles during the atomization process is released during melting and incorporated by the MP, forming spherical pores. SLM systems either employ inert gases to prevent contamination, typically argon, which are insoluble in liquid metals, hence forming pores whenever the gas is unable to escape the MP, or employ N_2, which is known to reduce porosity in stainless steel welds by dissolving into the liquid before it solidifies. However, nitrogen may react with the metal and act as austenite stabilizer [16, 37].

Heat-input and melt flow process-induced porosity is related to MP shape instability, through excess heat input and/or scan speed, causing spheroidal/hemispheric pores, or to insufficient heat input causing irregular, lack-of-fusion pores. High laser power expands the MP, thus enhancing heat penetration. However, high scan speeds, at constant power, hinders it and promotes unpredictable melt flow, possibly generating pores, spattering, and denudation zones [16, 36, 37, 42].

High heat-input process-induced round pores originate from excessive heat input through incorporation of ambient gas, or the gas mixed with the powder or vaporized alloy within the MP, as it has no time to escape when the MP cavity collapses [36]. Under excessive applied energy, melting is performed in keyhole mode, leading to spatter and keyhole pore formation, whereby the successive collapse of the cavity produces a trail of voids

along that vector [43]; these voids are typically rounded since they form by gas entrapment, whose pressure determine the pore shape (Figure 10).
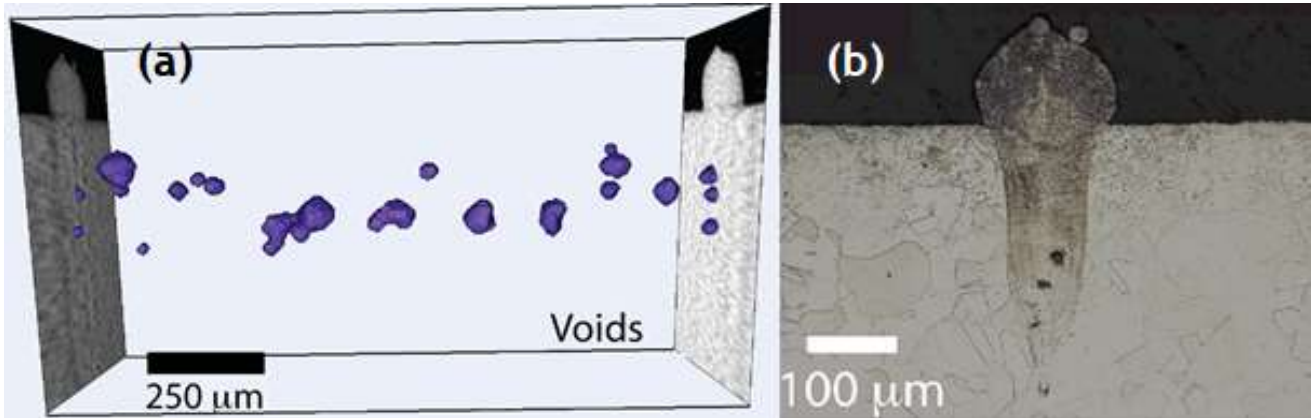
Figure 10 : SRµT image (a) of the porosity trail formed during keyhole-mode laser melting, (b) cross-section metallographic image of the single-track analysed in (a) [43].

Thijs *et al*. [41] reports keyhole pores at the end of scan tracks which khairallah *et al*. [36] correlate to a sudden (1 µs) laser switch off (Figure 7b). As previously described in section 2.4.3, the sudden removal of the RP sustaining the depression causes its instant collapse, possibly forming ellipsoidal/hemispheric pores at the vector's end.

As the laser travels, RP pushes the liquid against the depression's inner front, thus accumulating at the rim, feeding a liquid wave front from which spatter emerges. The surface vapor flux within the MP, a gas plume escaping the cavity, compresses and elongates the liquid, which separates into droplets due to ST, that may be projected away if enough kinetic energy is imparted by the vapor flux, effectively removing material from the MP and promoting porosity [36].

Irregular pores induced by low heat-input occur if the energy effectively transferred to the powder is too low to achieve enough heat penetration for complete fusion between particles and already consolidated metal. Lack-of-fusion irregular pores may also form through the interplay of surface tension, melt flow and wetting conditions with the local stochastic powder configuration or consolidated metal and incorporation of partially melted particles [16, 36, 42].

Irregular pores may form with a myriad of shapes and be much larger than gas related ones, over 10 µm in equivalent diameter. Lack-of-fusion between spherical particles and between these and consolidated material, incorporation of partially or un-melted

particles, with necking between them, and respective voids, create very irregular delineations with sharp edges, which act as stress concentrators under applied loads and residual stresses. These pores may also be identified by observation of unmelted particles within the voids (Figure 11), adhering onto its walls [16].

Since these pores are associated to insufficient heat penetration, they may also present a preferential distribution [10, 13, 46], seemingly aligning with scan vectors or laser manoeuvres (like island corners or U-turns of the laser) forming broadly elongated or highly curved or jagged pores; also, these may be connected.

| (a) | (b) | (c) |
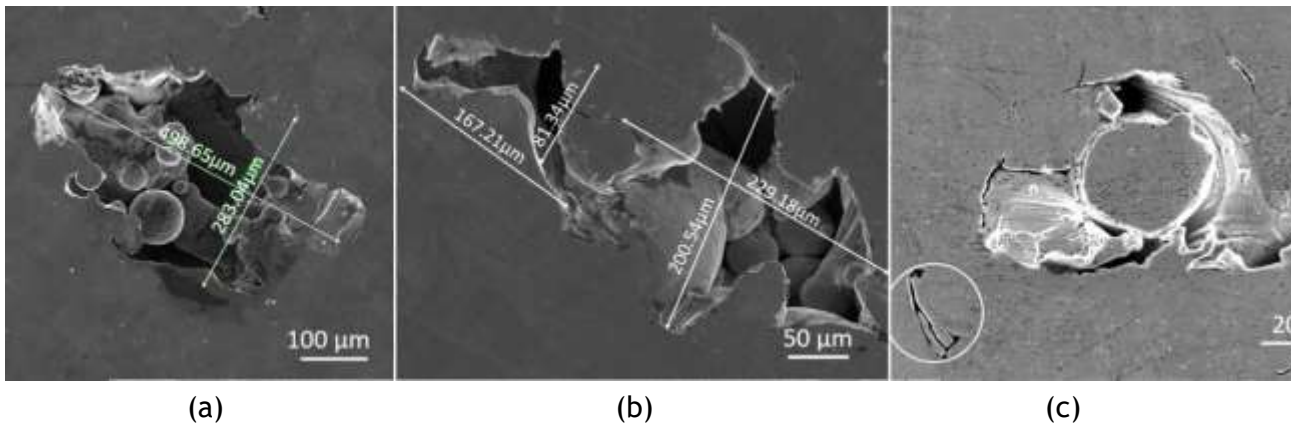
Figure 11: Porosity caused by lack-of-fusion [16].

Denudation zones are characterized by the depletion of powder particles in small areas along the sides of the MP. The liquid that circulates at high speed (1-6 ms^{-1}) around the rim of the depression exceeds the track width and can capture adjacent particles and drag them into the MP transition zone. These particles usually melt completely but may melt partially, necking with the track and affecting heat and mass flow by ME. The lateral bridging between particles and the transition zone may create gaps underneath and the incorporation of partially melted particles, and the voids formed between them, may translate to shallow lateral pores [36].

Gu *et al*. [16] used an EOS M270 to process 17-4PH steel and evaluate the effect of energy density ($E = P/Vht$) on porosity. For samples produced with varying E (41 to 81 Jmm^{-3}) by changing scan speed at constant laser power (195 W), only the sample processed with the highest (1200 mm/s) speed exhibited porosity above 0.4 % (1.3 %), from relatively small pores with very few unmelted particles, but more cracks. Samples produced with varying laser power and scan speed to keep optimal E (61 Jmm^{-3}) exhibited significantly different

levels of porosity, up to 5.4 %, when both laser power and scan speed were lowest. Despite *E* being kept at the optimum level, the presence of large caves and crevices with many unmelted particles suggests that *E* may not be a reliable indicator for porosity in SLM.

Gong *et al.* [42] used an EOS M270 to study the influence of varying energy density ($E = P/Vht$) through scan speed on porosity of Ti–6Al–4V alloy. Samples produced with optimized parameters (*E*=42 J/mm^3) exhibited no major defects, except for some sparse pores. When the energy density is increased (*E*=74 J/mm^3), the samples developed small round pores (>50 μm) (Figure 12a), that became larger (up to ~70 μm) with further increase in the energy density (*E*=100 J/mm^3) (Figure 12b). Similarly, when *E* was reduced to 32 J/mm^3, the samples developed slightly more irregular and larger pores (up to 110 μm) (Figure 12c) than those found in the samples exposed to 74 J/mm^3, and further decrease in the energy density (27 J/mm^3) generated more irregular, numerous, and larger (up to 250 μm) pores (Figure 12d).
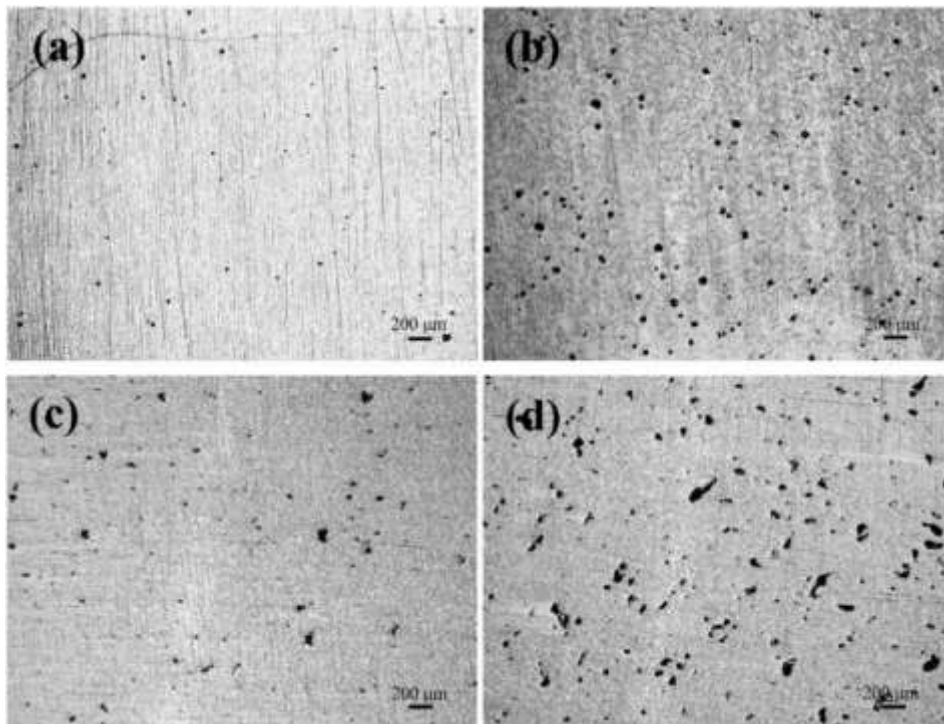
Figure 12: Excess (a-b) and insufficient (c-d) heat input porosity with varying energy density [42].

2.6.2 Balling

Balling refers to the segmentation of the MP into spheroidal beads instead of forming a continuously consolidated track, or by separation of smaller melt spheres from the MP,

which are dragged by the Marangoni flow to the side edges of the track where they solidify, generating porosity and surface roughness [37].

Balling is the manifestation of a variant of the *Plateau Raleigh capillary instability*. This phenomenon arises from instability of the MP due to surface tension and insufficient wetting between the liquid metal and the preceding layer [47, 48]. At high scan velocities, the MP tends to elongate and become unstable, forming a half-cylinder that separates into spheres to maintain the uniform capillary pressure within the MP [49]. Based on the *Plateau Raleigh instability*, the length to diameter ratio of the MP should not exceed π. The local powder arrangement may also influence balling by disturbing the MP shape; smaller particles and higher packing density mitigates the effect. Gu *et al*. [26] studied balling on 316L processed by DMLS and found that low energy density generated coarse balling, whilst high energy density resulted in a large number of finer spheres (~10 μm).

Li *et al*. [50] investigated the balling phenomenon with 316L and Ni and the influence of differing oxygen content, layer thickness, scan speed and power. They observed large (~500 μm) ellipsoidal pellets due to a lack of wettability, which are detrimental to the process, and small spherical pellets (~10 μm) with no identifiable harmful effect. Enhanced wettability between the MP and the substrate was achieved by restricting oxygen content of the atmosphere below 0,1 vol% and applying high beam power with low scan speed, regardless of hatch spacing [50]. This can be explained by the oxide film on the underlying layer since liquid metals generally do not wet oxide films in the absence of a chemical reaction [47, 48]. Re-melting can mitigate balling by destroying the oxide film; increasing layer thickness (>0,1 mm) promotes it [50].

2.6.3 Cracking

There are different mechanisms by which cracks form in MAM samples where micro-defects act as crack initiators under the influence of residual stresses generated by the large thermal gradients. However, the observed correlation between applied energy and void density is yet to be made with crack density [37, 40]. Crack length varies widely; possibly occurring within layer thickness or spreading across several layers [37].

Solidification cracking (hot tearing) occurs within the solidifying MP; it is dependent upon the solidification mechanism (dendritic, cellular, planar) and associated to higher energies. If high enough energy is applied, great thermal gradients may cause high strain

within the MP due to solidification shrinkage and different thermal contraction between solidified and yet to solidify material and between the cooling MP and underlying solid material. These thermal gradients generate a tensile stress at the solidifying layer. Moreover, an insufficient supply of liquid during solidification may occur due to flow obstruction by solidified grains, whereby the remaining liquid act as crack initiation points, under stress, during solidification [40].

Grain boundary cracking nucleates and propagates along grain boundaries; it is associated with lower energy densities and depends on the material since it results from phase precipitation and grain boundary morphology, which are the most significant alloying element segregation areas. Carter et al. [40] suggests three mechanisms for this phenomenon. *Liquation cracking* occurs in the partially melted zone and arises from the tendency of certain grain boundary phases, like eutectics and carbides, to melt when the material surrounding the MP is heated rapidly below the overall liquidus of the alloy, thus acting as crack initiators, triggered by residual stresses. Alloys with large difference between liquidus and solidus temperatures, solidification shrinkage and coefficient of thermal expansion are most susceptible to the phenomenon. S*train age cracking* is also related to the process heating cycles, leading to the precipitation of hardening phases, which associated to residual stresses promote the brittleness of grain boundaries. *Ductility dip cracking* arises from the brittleness of certain materials at specific temperature intervals.

2.6.4 Residual Stresses

Residual stresses are stresses that remain within the material in the absence of external forces or thermal gradients. Macroscopic residual stresses vary over the dimensions of the parts, affecting their bulk performance. These can trigger failure from structural defects, hamper mechanical properties or act as the driving force for microstructural changes. Induced stresses exceeding local yield stress will result in plastic deformation, and if those exceed local UTS, cracking may occur. Average tensile residual stress measurements on SLM processed MS may exceed 700 MPa [13].

There are several factors contributing for the generation and accumulation of residual stresses. Large and localized spatial thermal gradients are inherent to MAM processing as the fast-moving heat source creates localized differential heating and cooling of solid

material during and after solidification, leading to differential thermal expansion and contraction, more so with large CTEs [51].

The first mechanism inducer of residual stresses is the thermal gradient mechanism (TMG). TMG results from large thermal gradients around the laser spot due to the rapid heating of the irradiated top surface, as compared to the slow heat propagation to the underlying material. While the strength of the material decreases from the temperature rise, the expansion of the top layer is restrained by the underlying material, thus introducing an elastic compressive stress which will result in a plastic compressive strain once the yield strength is reached. This mechanism does not require the top layers to be molten. During cooling the molten top layers shrink due to solidification shrinkage and thermal contraction, which is again inhibited by the underlying material, thus introducing tensile stresses in the added top layer and compressive stresses below [51].

Macroscopic residual stresses tend to be large and tensile (close to yield stress) at the top surface of SLM parts, with balancing compressive stresses in the centre, and lower tensile stresses at the free edges, which are concentrated near the substrate interface before its removal [51, 52, 53]; these stress configurations are also linked to the skin and core scanning modes in larger structures, where increasing volume to surface ratios leads to increased differential between compressive interior and surface tensile stresses [52]. Neutron diffraction measurements found peak tensile residual stresses near the top surface and constant compressive stresses 2-3 mm into the core [52].

The laser spot energy density distribution and the orientation of scan vectors can alter the residual stresses configuration, and to some extent, it's intensity within a layer, but has no effect on axial residual strains [54]. The thermal profile generated by the laser depends upon the material [35], also, certain materials undergo phase transformations that may also induce microscopic residual stresses. Residual stresses mitigation methods include: support structures between the part and the substrate [51] and pre-heating the base plate [55]; re-melting, heating the powder bed or holding (steel) for 1h at 600-700 ºC, or 1 hour at 830 ºC for MS [13], can reduced residual stresses by 55, 40, 70, 80 %, respectively [56].

2.7 Structures

MAM metallurgy is mostly driven by feedstock chemistry and thermal history. Heat source characteristics and parametrization, together with material thermo-physical properties and macrostructure, determine heat absorption and transfer, which in turn induce mass transfer and flow, thus defining MPS. Solidification kinetics is mainly controlled by MP kinetics and geometry, thereby determining phase formation and initial distribution, and grain structure. The scan strategy will affect thermal distribution, cycles and history, which, with cooling path, determine further precipitation kinetics, phase and grain growth.

As previously explained, recoil pressure induces highly complex and dynamic melt flows within the MP, which, along with the huge thermal gradients and 3D transient temperature distributions, result in non-equilibrium solidification conditions of high solid solubility and low solute partitioning. These conditions create highly refined heat flow-oriented structures and possibly the formation of metastable phases.

Most MAM processed materials exhibit a bulk structure partitioned by melt pool boundaries (MPB) and MP overlaps, and consequent surface defects with an apparent influence on porosity and chemical distribution. The highly refine grain structure is heat-flow-oriented, i.e., normal to MPBs, delineating the molten pool with submicron columnar or cellular grains, whose orientation typically extends across the MPB by epitaxial growth from the solid-liquid interface between the MP and previously consolidated underlying tracks, including re-melted portions of the latter.

2.7.1 Thermal Fluctuations and Process Thermal History

AM entails simultaneous and reiterated partial melting of adjacent consolidated tracks, beside and below each new track. Unlike most other materials processing methods, each location of the part experiences multiple temperature peaks and thermal cycles of high heating and cooling rates from the heat affected zone of the laser. This thermal fluctuation has been experimentally measured and digitally simulated. Furthermore, variations in part geometry, scanning parametrization and sinuosity create considerable local variations in heat flow, ultimately generating complex and continuously changing thermal profiles within the build. Depending on the amplitude of the thermal fluctuations

and on the chemistry of the material, a point of the part may experience reiterated solid-state reactions and liquid-solid transitions. The conjunction of repeated thermal oscillation, fast cooling and directed heat flow largely dictate the resulting microstructure. Reiterated thermal cycles with varying scan vector orientations creates a complex thermal history which may result in considerable microstructural differences between layers. Since the substrate acts as a heatsink, the conduction heat-loss decreases with increasing layer number, reducing the cooling rate and G/R ratio. These factors increase MP size and the peak temperature of the upper layers, consequently generating location-dependent microstructural and property inhomogeneities.

2.7.2 Solidification

The MP dissipates the heat to the surrounding material creating an elongated hemispheric MP whose geometry is key for the resulting structure. Broadly, in conduction mode, the MP has a tear-drop shape as seen from above and sides, and a parabolic frontal outline. MPS varies with processing parameters, mainly laser power and speed, through the complex interplay of several phenomena like wettability, capillarity, surface tension, Marangoni effect, and recoil pressure. The combined effect of these phenomena affects heat flow and consequent temperature field, especially at the MPB, hence local temperature gradient and solidification rate, which translates to grain structure.

SLM processing typically occurs between room temperature and 200 ºC, while materials exceed boiling temperatures and the MP solidifies in seconds. SLM experience the highest cooling rates in MAM processing due to the high scanning velocities and no pre-heating. Literature reports values from 5×10^5 to 6×10^6 Ks^{-1}, which are crucial between the liquidus and solidus temperatures where solidification microstructure is determined, or where thermal history determines the extent of solid-state transformations. As an example, for steels this cooling rate is important between 800-500ºC where the cooling rate greatly affects microstructure [37].The local solidification growth rate, R(cm.s^{-1}), the temperature gradient, G(Ks^{-1}), at the solid-liquid interface, and undercooling ΔT are the most important parameters that affect the solidification structure [57].

2.7.3 Solidification Structure

A solidification map (Figure 13) may be constructed from the G/R ratio, which determines the morphology/mode of solidification, i.e. planar, cellular, columnar dendritic or equiaxed dendritic, with decreasing G/R values, and the GR product, which controls the scale of the solidified microstructure, decreasing with increasing cooling rate, and enables the prediction of SDAS of columnar and equiaxed dendrites. These factors enable control over the transition from epitaxially growing columnar dendrites to equiaxed dendrites; the columnar to equiaxed transition (CET) [9, 37].

(a)   (b)
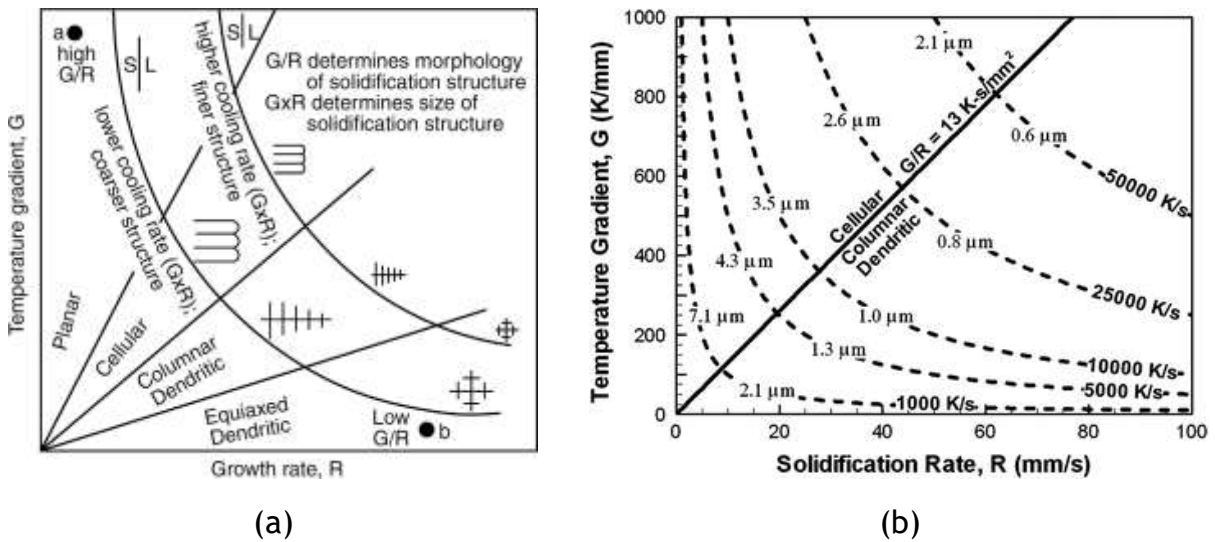
Figure 13: (a) Effect of G and R on the morphology and scale of solidification microstructure; (b) Solidification map for laser welding of the IN690 alloy showing the transition from cellular to columnar dendritic morphology with various cooling rates; along each cooling rate is the cell spacing and SDAS [58].

The driving force (or Gibbs free energy difference) for dendritic growth is proportional to the undercooling, which is the difference between the equilibrium liquidus temperature and that of the local dendrite tip. For most metallic alloys solute undercooling (constitutional supercooling) is the predominant component of the total undercooling which increases growth rate thus impacting microstructure [37].

Re-melting of previously deposited layers removes surface contaminants, breaks down oxide films, and provides a clean solid-liquid interface at the atomic level, thereby allowing epitaxial growth (Figure 14) and interlayer consolidation. This eliminates the nucleation activation energy barrier providing spontaneous growth at the MPB.

Although the base metal determines the solidification structure at the MPB by epitaxial growth, further away from the MPB the microstructure is dominated by competitive growth. In iron-based alloys, this occurs between dendrites with various crystallographic orientations, whereby those having their preferential directions ((100) for fcc and bcc structures) most aligned with the maximum heat flow direction will prevail [59]. At the MPB, preferential growth of previously deposited grains will occur when those oriented along (100) happen to be closely aligned with maximum heat flow. Since the heat flow at the MPB is dependent on its local curvature, normal to the solidification surface, it will affect the direction of local columnar structures.
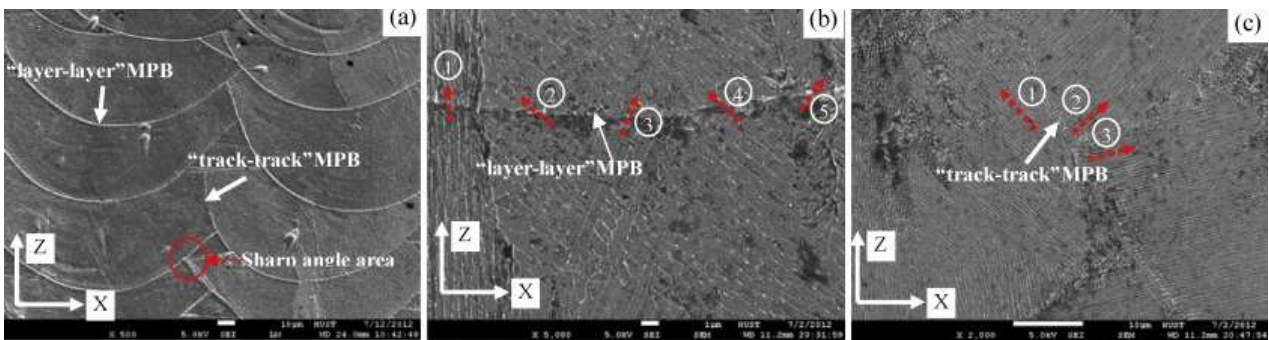
Figure 14: SEM images of a transverse MP cross-section in SLM processed 316L samples: (a) MPBs; (b) epitaxial growth at "layer–layer" MPB; (c) grain orientation at track–track MPB [60].

Local grain growth rate depends on scan speed and on the location at the MPB, increasing as grains approach the centreline of the MP and with scan speed. However, LPBF systems operate at too high scanning speeds for the solidification front to match it, the difference being strongly dependent on the thermo-physical properties of the material and processing parameters [37].

2.7.3.1 Grain Structure

The observation of the MP structure and grain orientation depends on the cross section, i.e. transverse, longitudinal or horizontal. Depending on the thermal properties, the relatively high scan speeds and small beam diameter used in SLM result in relatively long and shallow MPS with high length to width ratio (5:1) and length to depth ratio (20:1) [37].

Low inclination bottom MPB ensure near directional solidification conditions in the central longitudinal plane, where grains grow predominantly aligned with building direction and maximum heat flow, i.e., nearly vertical columnar grains epitaxially growing with the rising solidification front. The transverse MP cross-section has a low aspect ratio parabolic

delineation, along which the difference between the maximum heat flow direction and the normal to the MPB increases from the bottom. The resulting grain growth orientation may deviate significantly from building direction, particularly when grains grow perpendicularly to the MPB at track-track MPB; this is potentiated by epitaxial growth and lateral heat flow. Grain growth direction may have a slight tilt towards scan direction if scan speed is low enough to produce an inclined trailing solidification front [37, 41].

Cooling rate dictates grain size in MAM. Higher cooling rates yield finer grain structures by providing shorter growth times. Cooling rate decreases as the layer height increases due to the accumulation of heat during the AM process, coarsening the microstructure at the upper layers. Re-heating cycles induced by scan strategy promote grain growth; continuous competitive growth results in fewer, larger grains. Grain morphology is either columnar or equiaxed. Highly oriented columnar structures exhibit high mechanical anisotropy. Texture is highly dependent on scanning parameters, especially scanning strategy and raster relative direction and orientation between layers. A strong (001) texture is common since it is parallel to build direction but also a compromise result of grain growth [37].

2.7.4 Maraging C-300 Structures

2.7.4.1 As-built

As-built MS processed by SLM exhibit a typical MPB-partitioned structure, with similar maximum width as the laser spot, and overlapping half-ellipse (parabolic) shaped cross-sections of the tracks in side-view, with a height similar to the layer thickness. Casati *et al*. [15] describes a similar track cross-section structure to those obtained by a continuous laser in side-view, whereas in top-view, one can see distinct pools pertaining to different layers on the same track as consequence of the discontinuous melting process induced by the pulsed laser beam. Obviously, the exact configuration of this mesostructures depends on layer-layer relative scanning strategy.

SLM processing entails very high cooling rates; the fast solidification prevents formation of lath martensite. Some authors [10, 11, 13] describe a fine cellular/dendritic grain structure, while others [14, 15, 45, 61] report a fine cellular grain structure; Jägle *et al*. [61] point out that it is unclear if the observed structures are solidification cells or

dendrites with very short SDAS. OM and SEM image observations suggest microstructures composed of either columnar or equiaxed cell domains. All 18Ni-300 MS SLM studies report SEM assessments of fine elongated cells with intercellular spacing under 1 μm, mostly aligned with heat extraction at layer-layer boundaries where copious observations of epitaxial growth have been made.

2.7.4.2 Heat Treated

The microstructure of aged SLM-processed MS differs significantly from that of MS produced by conventional methods. The former contains nanoscale intermetallic precipitates dispersed within fine (~1 μm) cellular grains while in the latter the precipitates are dispersed through martensitic laths (0.5-1 μm) within prior-austenitic grains (30-50 μm) [45].

Aging does not appreciably alter the as-built microstructure while solution annealing replaces it with a martensitic structure. Thorsten *et al*. [13] solution-treated samples for 1 hour at 830 ºC, thus replacing the fine cellular structure by a martensitic lath matrix; aging accentuated the coarsening of the solution annealed microstructure. Casati *et al* [15] solution-annealed samples for 30 minutes at 850 ºC resulting in a complete loss of their cellular solidification microstructure, which was replaced by coarse martensite, described as consisting of massive blocks of fine bundles of parallel, heavily dislocated laths, as assessed by EBSD analysis. Crystallographic data shows traces of reversed austenite mostly dispersed on the boundaries of the martensite blocks. Solution annealing lowers hardness significantly (table 1) probably due to the microstructural coarsening and residual stresses relieving, rather than an intrinsic aging effect of the SLM process [61].

2.7.4.3 Overaging

The aging treatment of 5 hours at 480 ºC performed by Kempen *et al* [11] resulted in an increase of austenite (fcc) content from 5.8 vol%, present in the as-built condition, to 9.4 vol%. Casati *et al*. [15] measured over 11 vol% of austenite in the as-built condition; XRD and SEM observations reveal an increased amount of austenite at the cell boundaries of aged samples, and overaging leads to massive thickening of this phase and its intragranular precipitation. Temperature creates a higher austenite reversion rate than time, exceeding 17 % after 10 minutes at 600 ºC contrasting with the 15 % measured after aging at 460 ºC for 8 hours. Also, ductility does not benefit from a higher austenite content [15].

2.7.4.4 Precipitation

Jägle *et al*. [61] studied the precipitation behaviour of SLM processed MS. APT analysis was performed perpendicularly to building direction, at the centre of the scan track. In the as-built condition, results show high similarity of the overall concentration of major elements relative to powder chemistry. 3D atom-maps and nearest-neighbour distance distributions exclude any precipitation, clustering or incipient nucleation. SEM images of aged samples show the development of new phases within and at the boundaries of the cells, the latter identified by EBSD as austenite. APT atom maps clearly show precipitation zones with regions enriched in Ni, Mo, Ti and Al and depleted of Co. Three different types of precipitates were found after aging that presumably precipitate in this order: $(Fe,Ni,Co)_3(Ti,Mo)$, $(Fe,Ni,Co)_3(Mo,Ti)$ and $(Fe,Ni,Co)_7Mo_6$ or (µ phase). The first are the most frequent, nearly equiaxed in shape and have a 2-7 nm diameter; the second are fewer and elongated, these precipitates form an interconnected network and are oriented along preferred directions; the third are scarce, equiaxed and 5-11 nm in diameter, usually located at the corners or nodes of the $(Fe,Ni,Co)_3(Mo,Ti)$ network, which may have acted as nucleation sites for this Mo-rich phase. Retained austenite was also detected; reverted austenite forms a thin, Ni-rich, shell around regions of retained austenite [61].

2.8 Properties

Given the specificities of SLM-produced microstructures, these exhibit some differences in mechanical properties when compared to wrought or casting parts. The SLM components yield higher tensile strength, lower ductility and strong anisotropy associated with building direction. The YS, UTS and hardness of the SLM as-built parts are higher than those of wrought parts due to residual stresses and oriented fine microstructure, but comparable after heat treatment. Anisotropy depends on the material but also on residual stresses and microstructure, so it varies with scanning parameters. SLM parts exhibit lower (and anisotropic) fatigue performance due to porosity, residual stresses and surface condition. Surface roughness and dimensional accuracy are like precision casting but lower than machining and precision forging. Properties inconsistency within and between builds, machines and techniques, as well as process-induced defects and location/orientation-dependent properties are the major drawbacks [17, 37, 62, 63].

As-built SLM-processed MS exhibit higher hardness, YS and UTS than wrought solution-annealed MS, especially if re-melted (table 1); this difference is lost upon annealing. Reported elongation values for wrought solution annealed MS vary considerably (6-15 %), yet, apart from Casati *et al*. [15], as-built SLM elongation data consistently exceeds 10 %. Hardness and tensile results obtained from aged SLM-MS are similar to those reported for wrought aged MS; in contrast, elongation is especially lower when compared to wrought aged products. Re-melted aged parts may yield slightly higher hardness and UTS [10, 11]. Suryawanshi *et al*. [45] reports similar fracture toughness and fatigue crack growth characteristics between aged SLM and wrought MS. Tensile testing results from MS samples built perpendicularly or parallel (horizontal samples) to the powder bed are alike [13, 45]; EOS [17] claims anisotropy can be reduced or removed through solution annealing (table1).

Table 1 : Mechanical properties of wrought and SLM-processed Maraging C-300 steel.

	Heat Treatments	Hardness	YS (MPa)	UTS (MPa)	e (%)	E (GPa)
[7] (wrought)	1h @ 815 ℃	30-37 HRC	760-895	1000-1170	6-15	-
[6] (wrought)	1h @ 820 ℃ + 3h @ 480 ℃	-	2000	2050	7	-
[17] EOS equivalent parameter sets: MS1_040_default.job or MS1_Performance 2.0. (40 μm layer thickness)	As-built	33-37 HRC	(XY)1100±100; (Z)930±150	(XY)1200±100; (Z)1100±150	(XY)12±4	(XY)150 ±25; (Z) 140±25
	2h @ 940 ℃ + air cooling + 6h @ 490 ℃ + air cooling	50-57 HRC	(XY)2010; (Z)2000	(XY)2080; (Z)2080	(XY)4; (Z)4	-
[10, 11] (re-melting)	As-built	39.9 HRC	1214±99	1290±114	13.3±1.90	163±4.5
	5h @ 480 ℃	58 HRC	1998±32	2217±73	1.6±0.26	189±2.9
[13]	As-built	~350 HV10	1080	1205	12.0	181
	As-built (HS)	-	1050	1100	12.1	194
	1h @ 830 ℃	~330 HV10	800	950	13.5	161
	6h @ 490 ℃	~600 HV10	1750	1850	5.1	217
	6h @ 490 ℃ (HS)	-	1720	1800	4.5	219
[14]	As-built	35-36 HRC	915±7	1165±7	12.44±0.14	-
	6h @ 490 ℃	51-55 HRC	1967±11	2014±9	3.28±0.05	-
[15]	As-built	371 HV2	915(13)	1188(10)	6.14(1.33)	-
	4h @ 490 ℃	605 HV2	1793(97)	1815(95)	1.20(0.13)	-
	8h @ 460 ℃	630 HV2	1957(43)	2017(58)	1.51(0.20)	-
[45]	As-built	-	826±96	1325±51	14.0±1.5	-
	As-built (HS)	-	768±29	1260±79	13.9±2.0	-
	5h @ 480 ℃	-	1833±65	2088±190	3.2±0.6	-
	5h @ 480 ℃ (HS)	-	1953±87	2216±156	3.1±0.4	-

(HS) – Horizontal samples

3 Experimental Procedures

3.1 Materials

3.1.1 Powder

Most GA particles composing the MS1 powder from EOS present spherical or near spherical shape, without sharp edges and with few satellites; sizes range from 6 µm to 60 µm and average 30 µm (Figure 15). Some clusters of coalesced particles and some elongated particles, exceeding 60 µm long, were also observed. Some inclusions were detected on particles surfaces which EDS reveals as very rich in O, Al and Ti. Table 2 shows the MS1 composition which is identical to that of Maraging C-300 steels.

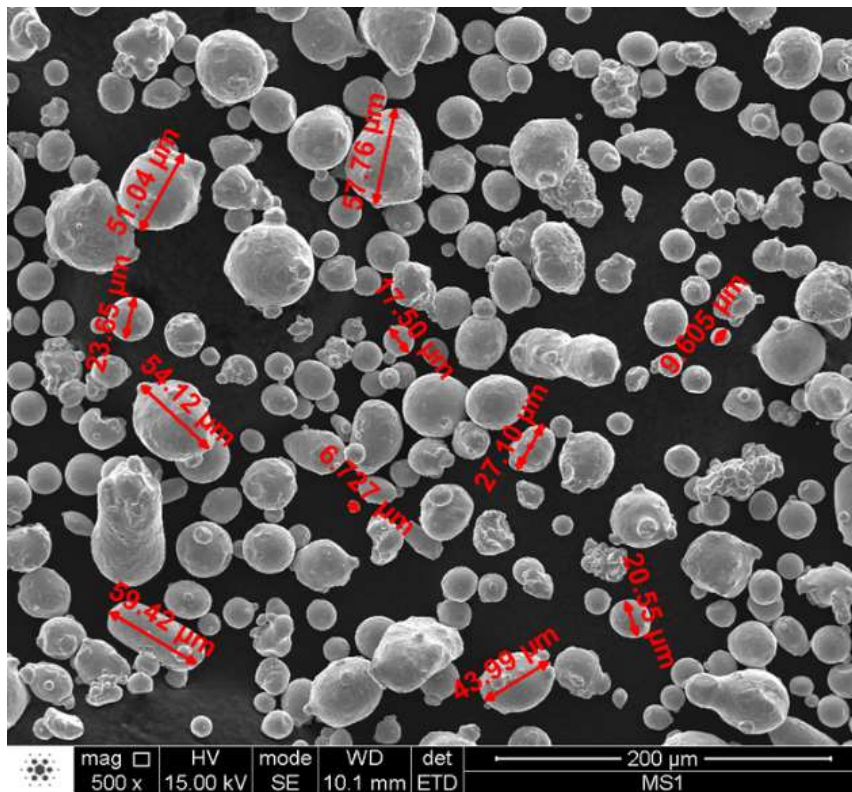

Figure 15: SEM image of MS1 powder.

Table 2: MS1 powder nominal composition.

Element	Fe	Ni	Co	Mo	Ti	Al	Cr, Cu (each)	C	Mn, Si (each)	P, S (each)
wt%	Balance	17~19	8.5~9.5	4.5~5.2	0.6~0.8	0.05~0.15	≤ 0.5	≤0.03	≤0.1	≤0.01

3.1.2 Parts

Parts used in this work came in two batches, from two different builds. All parts were in as-built condition and had been processed in N_2 atmosphere. The builds were performed by a company that owns the EOS M290 equipment, and the parameterization used was machine pre-defined by EOS for MS1 powder.

Four parts were available from batch one and used for testing of aging treatment conditions. These parts have specific geometry and dimensions because they replicate real, high consumption parts used in cable harness production. It is worth mentioning that the equipment showed an error halfway through this build (batch 1), which stopped it, and had to be resumed afterwards; this created a poorly consolidated zone, about 1 mm thick, that affected parts in different degrees depending on its position on the build table, and that has been characterized elsewhere. Parts studied here were also affected, but to a small extent, and the porous zone was removed while cutting the parts into small samples; over 2 mm of material adjacent to the affected zone was removed from the remaining two surfaces. The four test parts from batch one used in this study were designated as P1, P2, which are identical (40x20x3.43 mm); part Z, which is longer (75x20x3.33 mm), and X, which is longer and thicker (85x25x5.33 mm).

Batch two provided twelve tensile test samples and twelve Charpy test samples from a build that presented no processing issues; half of the tensile and half of the chock test samples were built vertically, with the longer axis parallel to building direction (z) and the other halves were built with the longer and shorter axis parallel to the powder bed (x-y). Tensile test samples had the following gauge dimensions: 8x12x55 mm.

3.2 Methods

The parts from batch one where first available and cut in small samples to test various aging conditions from which the one providing the highest hardness would be chosen to treat half the tensile and Charpy samples from batch two. The other halves were tested in as-built condition.

3.2.1 Test heat treatments samples (batch 1)

Parts P1 and P2 were identical. These were cut into 6 samples each, 8 of which were aged at 490 ℃ (group designated P490) for 3 to 10 hours (sample p493 to sample p4910, respectively) and 4 were aged at 460 ℃ (group P460) for 7 to 10 hours (samples p467 to p4610, respectively). Part X was cut into 12 samples, 5 aged at 490 ℃ (group X490) for 4 to 8 hours (samples x494 to x498, respectively) and the other 5 at 550 ℃ (group X550) for 1 to 5 hours (samples x551 to x555, respectively); the remaining 2 samples, x6 and x7, were analysed in as-built condition. Part Z was cut into 8 samples, half of which were aged at 510 ℃ (group Z510) for 3 to 6 hours (samples z513 to z516, respectively) and 4 at 530 ℃ (group Z530) for 2 to 5 hours (samples z532 to z535, respectively) (see table 3). The samples were aged in an electric resistance furnace, in air, with a heating rate of approximately 1.6 ℃.min^{-1} and cooled in still air to room temperature.

Table 3: Components sampling and heat treatments

Sample sets/ Time (hours)	1h	2h	3h	4h	5h	6h	7h	8h	9h	10h
P460 (7-10h)							p467	p468	p469	p4610
P490 (3-10h)			p493	p494	p495	p496	p497	p498	p499	p4910
X550 (1-5h)	x551	x552	x553	x554	x555					
Z510 (3-6h)			z513	z514	z515	z516				
Z530 (2-5h)		z532	z533	z534	Z535					
X490 (4-8h)				x494	x495	x496	x497	x498		

Top-view cross-sections of all samples were ground to 1000 mesh for optical microscopy (OM) analysis to assess the presence of porosity and inclusions and for hardness testing. Samples X490 were sectioned vertically and each half was mounted (together with x6 in side-view and x7 in top-view) so they could be inspected from side and top-view (normal to building direction z). Subsequently, side and top-view cross-sections of the X490 samples were polished to 1 µm diamond paste for SEM and EDS analysis, followed by etching (33 mL distilled water; 33 mL ethanol 96 %; 33 mL HCl; 1.5 g $CuCl_2$) for 4-6 s and rinsed with alcohol for further OM metallographic inspection. The electron microscopy and spectroscopy analysis were performed at Materials Centre of the University of Porto

(CEMUP) with a high-resolution SEM, FEI Quanta 400 FEG ESEM, while the composition was assessed with an energy dispersive X-ray spectrometer EDAX Genesis X4M coupled to the SEM. The EDS analysis were made at an accelerating voltage of 10 and 15 keV.

Vickers macro-hardness measurements (HV30) were conducted on all samples, except for Z510 and Z530, where such measurements were considered irrelevant. Indentations were done on a DuraVision 20 and the diagonals were measured by OM. Vickers Micro-hardness tests were also performed to avoid defects. Samples P490 were subjected to HV0.2 (0.2 Kg, 15 s) Vickers micro-hardness tests, the parts had a small cross-section area and defects had to be avoided. On every other sample HV0.5 (0.5 Kg, 15 s) measurements were performed, since the smaller indentation of the 200 g load hindered the accuracy of the measurement of the diagonals with the equipment used. Apart from z6 (as-built), all samples were observed and indented in top-view (surface normal to building axis-z). Samples X490 were also indented (HV0.5) in side-view; designated x494y to x498y, where mentioned. Prior to aging, p467 was also tested in the as-built condition (HV0.2 and HV30). At least seven indentations per surface were made.

3.2.2 Tensile Samples Heat Treatment (batch 2)

Tensile samples were aged at 490 °C for 6 hours in an electric resistance furnace, in air, with a heating rate of 1.6 °C.min⁻¹ and cooled in still air to room temperature. The tensile tests were performed at CINFU (Centro de Formação Profissional da Indústria da Fundição) according to ISO 6892-1:2012B, with a Shimadzu UH 1000KN. The tensile test samples were tested without any alteration to the surface condition. Charpy tests were discarded because the notches were too irregular to yield trustworthy results; in some cases, it did not even match the notch profile on either side of the same sample (Figure 16).
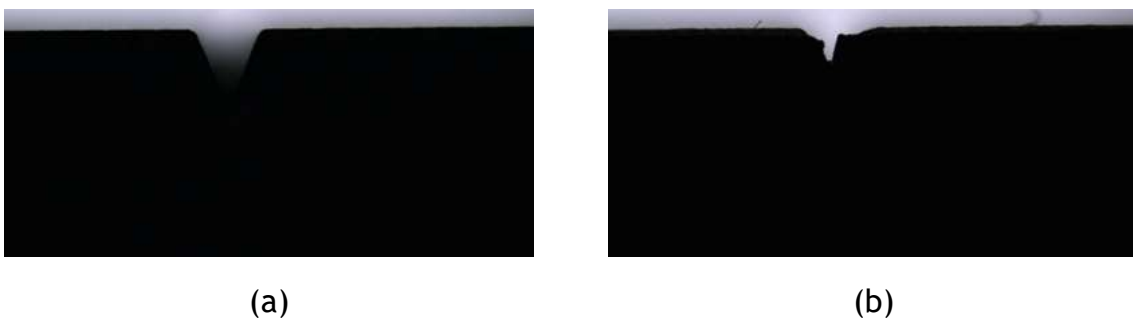

(a)   (b)

Figure 16: Notch profile as seen from each side of the same sample.

4 Results and Discussion

4.1 Properties

4.1.1 Hardness (batch 1)

Maraging C-300 steels processed by traditional metals typically present 300-350 HV hardness points in as-built condition [7]. The hardness values obtained from as-built samples (see Table 4) are similar to those found in literature for this alloy (table 1), processed by SLM, and slightly superior to conventionally produced MS.

Table 4: Hardness values from as-built samples

Vickers hardness test	As-built x467	As-built x7
HV0.2 (SD)	379.9 (6.53)	
HV0.5 (SD)		369.3 (4.92)
HV30 (SD)	372.1 (4.91)	

SD – Standard deviation

Maraging C-300 hardening relies on the precipitation of intermetallic phases at around 480 ℃. Regarding bibliography, 490 ℃ between 4 and 6 hours, or 8 hours at 460 ℃, without previous solution annealing treatment, seems to be the most promising aging parameters to maximize hardness, without re-melting by re-scanning. Casati *et al.* [15] reports 575HV at 540℃ for 1h and 525HV for 8h. Results shown in literature for heat treatments done at 480 ℃ relate to re-melted samples and the peak hardness is obtained between 5 to 8 hours without reported signs of over-ageing. Peak hardness measurements reported for temperatures above 490 ℃ are reached sooner but do not provide higher hardness values. Therefore, 490 ℃ was the primary temperature tested, and for a wide range of holding times, to assess which would provide highest hardness, and with that reference, choose the holding time ranges to test other holding temperatures. Temperatures above 490 ℃ would be tested with shorter holding stages relative to that which yielded peak hardness at 490 ℃ and lower temperatures would be tested with longer holding stages. Reported hardness results for samples treated at 460 ℃ for 8 hours exceed 600HV even without re-melting and seem to plateau without exhibiting over-ageing.

Solution annealing removes the as-built fine structure (section 2.7.4.2), reduces residual stresses (section 2.6.4) and minimizes tensile anisotropy [17], which would drastically interfere with the assessment of the influence of building direction on the anisotropic behaviour of the parts. Moreover, the priority was to maximize tensile resistance.

Table 5 presents the hardness results from all the heat treatments. Figure 17 presents a graphical representation of the micro-and macro-hardness results from all aged samples.

Table 5: Micro and macrohardness values (HV) from aged samples

Sample set/ load	1h	2h	3h	4h	5h	6h	7h	8h	9h	10h
P460/HV0.5							599(6.8)	604(8.4)	606(6.7)	608(4.8)
P490/HV0.2			596(7.4)	601(7.4)	611(6.1)	613(6.1)	608(6.6)	601(8.4)	597(8.9)	589(6.2)
X490/HV0.5				592(6.2)	598(4.9)	611(9.9)	606(8.9)	592(5.9)		
X490y/HV0.5				591(6.2)	595(9.3)	601(3.5)	587(7.1)	584(6.4)		
X550/HV0.5	532(6.5)	513(6.6)	500(7.4)	493(9.2)	488(4.6)					
Z510/HV0.5			579(3.9)	577(7.8)	578(9.5)	572(8.4)				
Z530/HV0.5		575(8.5)	570(6.6)	571(4.9)	569(3.5)					
P460/HV30							587(3.1)	578(5.1)	585(6.1)	579(6.6)
P490/HV30			583(6.0)	584(3.0)	591(7.1)	600(7.5)	599(6.9)	593(10.2)	588(5.0)	575(5.9)
X490/HV30				583(1.9)	585(2.9)	593(3.5)	582(5.9)	567(6.1)		
X550/HV30	517(3.6)	487(9.5)	485(5.3)	479(5.8)	481(2.9)					

() – Standard deviation

Aging at 490 ℃ provided the highest hardness measurements, approaching the highest reported values for samples built without re-melting. The hardness measurement sets from samples P490 yield the highest hardness for a 6 hours holding stage steadily decreasing afterward.

There is a significant difference, of 10 or more hardness points, between micro and macro-hardness results for each set of samples. This observation may result from the fact that the smaller the indentation the easier and more likely it is to avoid major structural defects, especially inclusions in this case, that may hinder the hardness measured; this precaution was taken, as much as possible, to assess the result of the heat treatment on the microstructure. Standard deviation is higher with smaller loads because the evaluation is more localized, reflecting the heterogeneity of the microstructure.

Micro-hardness values tend to result in smother hardness plot-lines whereas macro-hardness values of the corresponding temperature oscillate more. The components from which the test heat treatment samples were cut exhibited defects (oxide inclusions) in the bulk structure whose distribution varied significantly within parts; macro-hardness reflects that variability in defect density between the sampled surfaces of each part. This variance may indicate an inconsistency in processing conditions during the build.
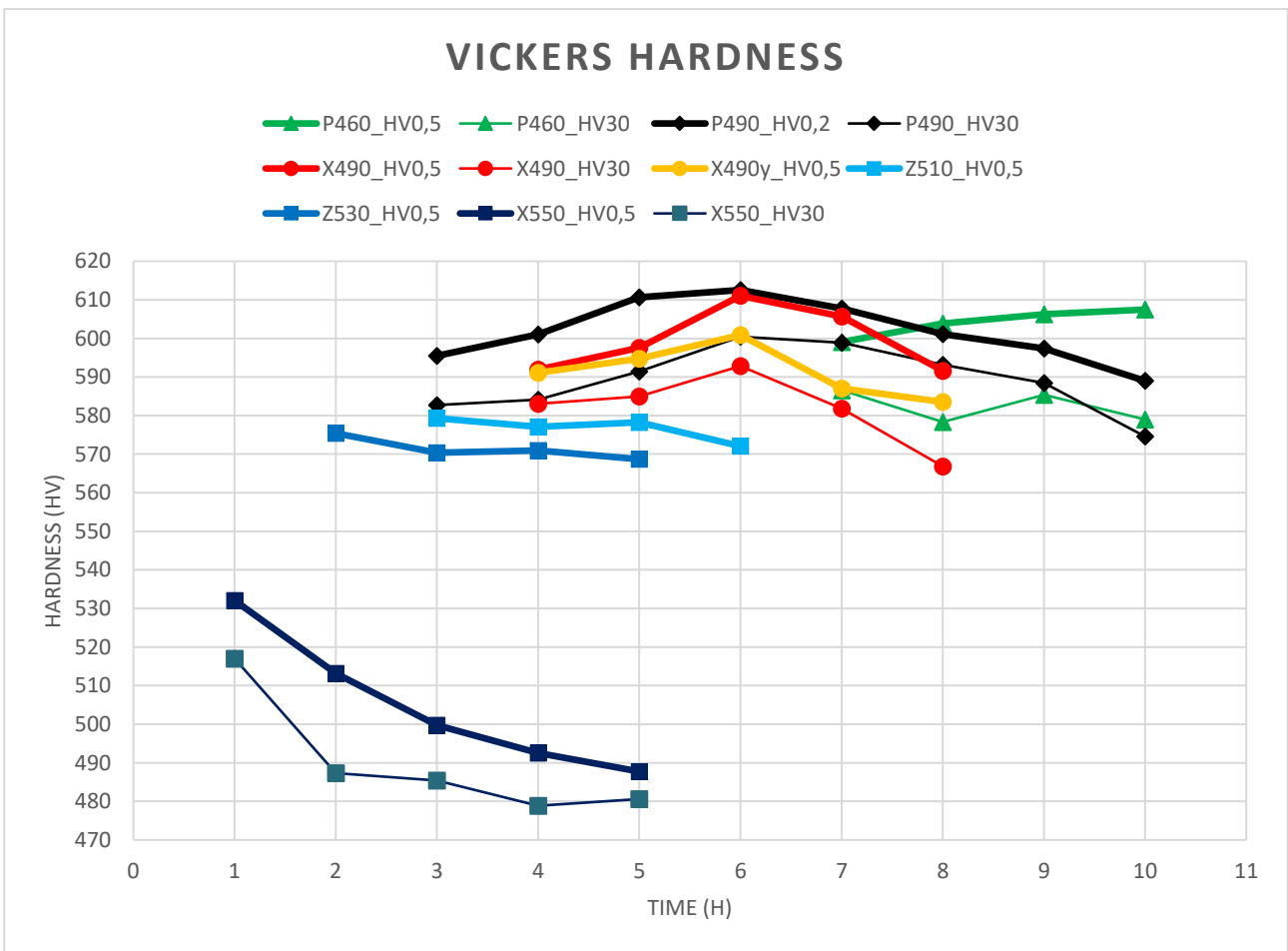
Figure 17: Micro and macrohardness obtained from aged samples.

HV0.5 testing of P460 samples shows no signs of overaging with hardness rising slightly up to 10 hours where it approaches the values obtained by Casati *et al*. [15] with a holding time of 8 hours. The asymptotic progression of the results suggests a stabilization of hardness with further aging, as expected from literature reports. The macro-hardness results are inconclusive since values vary around 582HV for the four holding times tested.

Considering the literature reports on the behaviour of SLM processed MS during aging for a set temperature, generally between 480 and 580 ℃, hardness increases quickly to a peak value and starts declining progressively afterwards. Furthermore, the higher the holding temperature the steepest the rise and decay of hardness values with holding time, most importantly, there is a temperature which yields the highest peak hardness. Heat treating at 490 ℃ for 6 hours resulted in the best performance in terms of hardness and time hence further test heat treatments would be performed between 490 and 550 ℃ for a holding time varying between 1 and 5 hours.

Aging at 550 ℃, considering literature, would probably not reveal a maximum hardness greater than that obtained at 490 ℃ but it provided a reference, along with the highest value from P490, for the establishment of the holding time ranges to be tested between 490 and 550 ℃ in order to determine if there is an aging temperature with a higher maximum hardness than that of samples aged at 490 ℃ for 6 hours. In contrast, aging between 460 and 490 ℃ was not undertaken since the highest values are very similar and the almost asymptotic behaviour of the 460 ℃ treatment curve suggests that aging between those temperatures would take more time to reach similar values.

The highest hardness measured after aging at 550 ℃ was reached with a holding stage of 1 hour, but it is much lower than the values attained in previous trials and declined steeply thereafter, indicating that peak values for that temperature may be reached before 1 hour, but not that it would reach the best values already measured for other temperatures, especially taking literature reports into account.

The next aging treatments would contemplate temperatures between 490 and 550 ℃, namely 510 and 530 ℃, to seek hardness values hopefully above the highest attained at 490 ℃. Since peak hardness for samples treated at 550 ℃ would likely be reached within a 1 hour stage, the highest of the two other temperatures to be tested started with a 1 hour holding period and up to 4 hours, while the other, closest to 490 ℃, started with a 2 hours stage and 5 hours for the longest, one hour below the best staging time for 490 ℃.

Both sets of samples, Z510 and Z530, yield their highest hardness for the shortest holding stage, declining slightly afterwards. The highest values measured are lower than that of samples aged at 490 ℃ and in hard contrast with the steep decline of X550 samples, suggesting that peak hardness for those temperatures was either reached on the first

stages tested or could be reached slightly sooner; probably with no significant gains in magnitude given the similarity of the values obtained with the tested holding times.

Finally, a set of samples from part X were aged at 490 ºC for 4 to 8 hours. These thicker samples provided a larger and cleaner of defects top-view surface and could be cut to allow hardness and metallographic analysis in top and side-view. The six hours holding time was confirmed as the most likely to realize the microstructure's potential as demonstrated by the hardness results of X490 and X490y samples depicted in figure 17.

4.1.2 Tensile Properties (batch 2)

The tensile properties measured are similar to those reported for conventionally built MS in as-built and aged conditions, except for elongation and Young's modulus, which are significantly lower and higher, respectively (see Table 6 and Figure 18).

Table 6: Tensile properties from batch 2

Condition/orientation		Rp0.2 (MPa)	UTS (MPa)	E (GPa)	e (%)
As-built/90	(M4)	1010.1	1085.9	263.4	7.2
	(M5)	1012.8	1080.1	264.4	9.1
	Average (SD)	1011.5(1.9)	1083.0(4.1)	263.9(0.7)	8.2(1.3)
As-built/180	(M10)	1110.0	1191.5	227.4	13.4
	(M11)	1099.7	1187.2	275.1	12.8
	Average (SD)	1105.2(7.3)	1189.4(3.0)	251.3(33.7)	13.1(0.4)
Aged/90	(M1)	1979.2	2016.0	308.3	ND
	(M2)	1973.1	2003.1	308.5	2.6
	Average (SD)	1976.2(4.3)	2009.6(9.1)	308.4(0.1)	2.6
Aged /180	(M8)	2010.0	2042.5	320.0	ND
	(M7)	1980.3	2014.2	305.0	5.4
	Average (SD)	1995.2(21.0)	2028.4(20.0)	312.5(10.6)	5.4

SD – Standard deviation; ND – Not determined

Tensile test results show that samples built horizontally (180) yield slightly superior results in as-built condition, except for Young's modulus which is particularly high in all samples and conditions when compared to literature and EOS's claims (table 1). The results from

aged samples are similar, but elongation, which varies considerably in literature, is very low, although consistently superior in horizontal samples for both conditions.
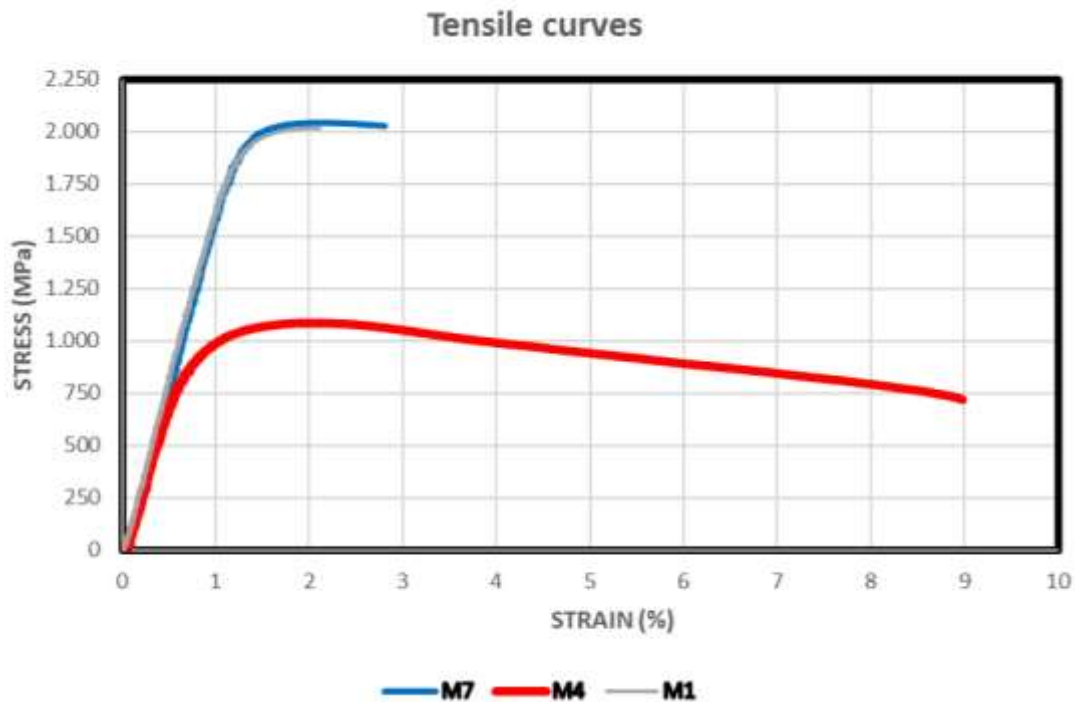
Tensile curves

Figure 18: Tensile test curves of samples: M4 (as-built, 90), M1 (aged, 90), M7 (aged,180).

Figure 18 shows the tensile behaviour of the samples M4, M1 and M7; highlighting the drastic difference between as-built (M4) and aged (M1 and M7) conditions. Literature fractography analysis of as-built tensile samples typically report evidence of a ductile failure mechanism, trans-granular dimple rupture [11, 14, 15], through microvoid nucleation, growth and coalescence. In the same surface, the equiaxed dimples vary significantly in diameter and depth; larger/deeper dimples, amidst shallow and much smaller ones, seem to nucleate in pre-existing defects such as unmelted particles and lack-of-fusion porosity [14, 15]. Aged samples undergo hardly any plastic deformation before rupture; although these feature similar fracture nucleation sites, fractography suggest a brittle failure mechanism, whereby cracks propagate through trans- and inter-granular cleavage [11, 14]. Casati *et al*. [15] observed longitudinal cross-sections of tensile samples near the fracture surface. They highlight the nucleation and propagation of large cracks through MPB in as-built structures and a trans-granular cleavage fracture in aged samples, with no noticeable contribution of reverted austenite at grain boundaries.

Regarding published results, MS do not show significant anisotropy (table1) [13, 17, 45]. Suryawanshi *et al*. [45] report that no anisotropy of the mechanical properties was found due to strong layer bonding and the absence of a dominant texture, since a preferred grain growth orientation was not observed, as confirmed by EBSD.

Wen *et al*. [60] studied the tensile behaviour of as-built SLM-processed 316L steel specimens built along several directions, including at 90 and 180 degrees to the powder bed, and the influence of the track-track and layer-layer MPBs. They report that parts built vertically have higher tensile strength and elongation, because tensile ductility of horizontal samples mainly derives from track-track MPB slipping while vertical samples benefit from slipping on both MPB types. The distance between track-MPBs is higher than that between layer-MPB, therefore, the vertical specimens have much more slipping surfaces per unit length. This was confirmed by fracture surface SEM analysis, however, Wen *et al.'s* [60] horizontal samples were built with a raster scanning pattern parallel between layers and perpendicular to the long axis of the tensile specimens while the samples tested here were built with a pattern that rotates raster direction by 67° between layers.

As previously mentioned, the relative orientation and direction of scan vector between layers has a great impact on texture and its homogeneity. If one considers a side-view cut-away of the MP (on the X-Z plane), as the laser travels from one side to the other, a cubic crystal cell at the longitudinal centreline of the solidification front that happens to have the (001) direction closely aligned with the (001) direction of the part (building direction), hence maximum heat flow direction, will benefit from preferential growth but will also most likely have a certain degree of misalignment with the part's (001) direction. When the laser travels in the opposite direction to melt the next layer, it will partially re-melt that crystal which has a slight angle relative to maximum heat extraction. Since the laser is travelling in the opposite direction the solidification front has a slight angle which is vertically symmetrical (on the X-Z plane) to the one it had before. Therefore, the new maximum heat extraction direction for that crystal, normal to the new solidification front, will now be misaligned by twice the misalignment angle it had previously. The combination of lateral heat flow, varying degree of grain orientation within each MP (highly oriented at the centreline and more chaotic near the lateral borders) and constantly changing

temperature fields, generate complex spatially evolving textures and accumulated stresses that influence the directional homogeneity of mechanical properties.

Anisotropy is also highly material-dependent. Hitzler *at al*. [64] compared the anisotropic behaviour of 316L SS and an aluminium-silicon alloy AlSi10Mg. The scan strategy was found to influence the material characteristics significantly. The evolution of tensile properties with the change of building inclination relative to loading direction is highly material-dependent; 316L SS yielded its maximum strength at a 45° layer versus loading offset, which is precisely where AlSi10Mg has been reported to yield the lowest results [64].

4.2 Structures

4.2.1 Surface Topology

All surfaces, from all parts, presented very distinctive surface topologies depending on their orientation relative to the powder bed. The vertical surfaces of samples from both builds displayed an accentuated layered topology, but the parts from the first batch had vertical faces particularly rough and of varying magnitude along the same surface. The horizontal surfaces on all samples were the smoothest despite the hilly topology, probably due to *up-skin* scanning (section 2.5.2). Top/side convex and concave surfaces were irregular and hilly/wavy, even presenting some incomplete structure covered by Ti-Al oxides, while overhangs were very rough and irregular probably due to melt interaction with underlying powder (Figure 19).

Top, down and inclined/curved surfaces are built through *up-skin* or *down-skin* re-melting which is supposed to smooth the surface and mitigate the layering effect. However, this may cause overheating in thinner sections because of the short scan vectors entailed (section 2.5.3); furthermore, bi-directional raster scanning with 67° rotations will lead to very short vectors at the corners of the parts.

Vertically built samples exhibit a lengthwise surface colour gradient reminiscent of the colours produced by interference phenomena between light and titanium oxides, mostly amorphous TiO_2 (anatase), occurring at the metal–oxide and oxide–air interfaces. The Ti oxide films obtained from high temperature oxidation or laser irradiation may be amorphous or crystalline. The Ti oxide layer may form in a N_2 atmosphere with only traces

of O_2 and is mostly composed of TiO_2 within a mixture of other Ti oxides, as Ti_2O_3 and TiO. Ti_6O may also be present in the afore mentioned mixture if processing occurs under N_2 atmospheres with oxygen impurities and high enough temperatures (600 ℃ or more), in which case adsorption of nitrogen onto TiO_2 leads to the formation of titanium nitrides (TiN and Ti_2N), which affect the optical properties of the oxide film. The crystalline structures form at higher temperatures, between 400 and 600 ℃ depending on previous oxide film thickness; a mixture of both forms may exist between those temperatures and the crystallization of anatase into rutile (crystalline TiO_2) entails the loss of the interference colours. The colours are determined by the oxide film thickness, whose growth is highly dependent on temperature and little dependent on time [65].
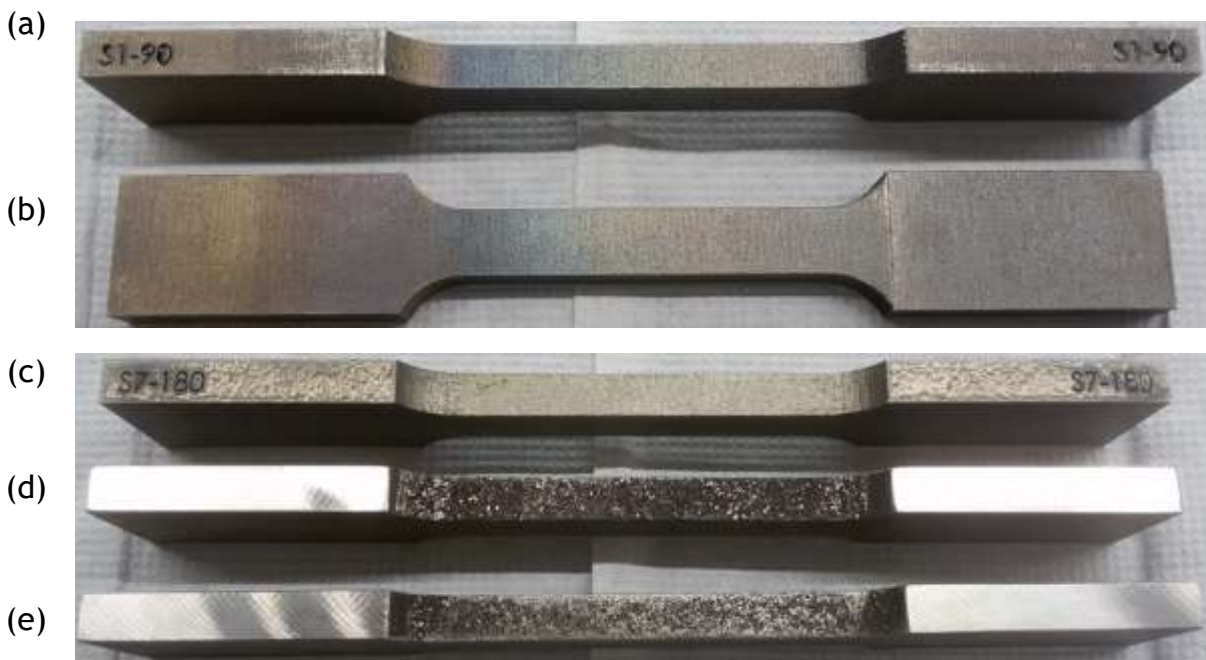

Figure 19: Tensile test samples surface texture: lateral surfaces of samples built vertically (a, b); top (c) and bottom (overhanging; d, e) surfaces of horizontally built samples (b).

4.2.2 Bulk structure

Figures 20a and b show a dark field top and side-view of sample x496, respectively. Etching reveals the mesostructure formed by the laser tracks and relative orientation. Track width is coherent with laser spot diameter and the angle between tracks of consecutive layers seems coherent with 67˚ raster scanning rotations (dashed lines in figure 20a).

The observable profile and dimensions of the tracks' transverse cross-sections may vary from layer to layer not only because of partial MP overlapping but also because the scanning vectors rotation between consecutive layers constantly changes the angle of the cross-section observed relative to track vector; consequently, every few layers some laser tracks are visible in longitudinal cross-section.
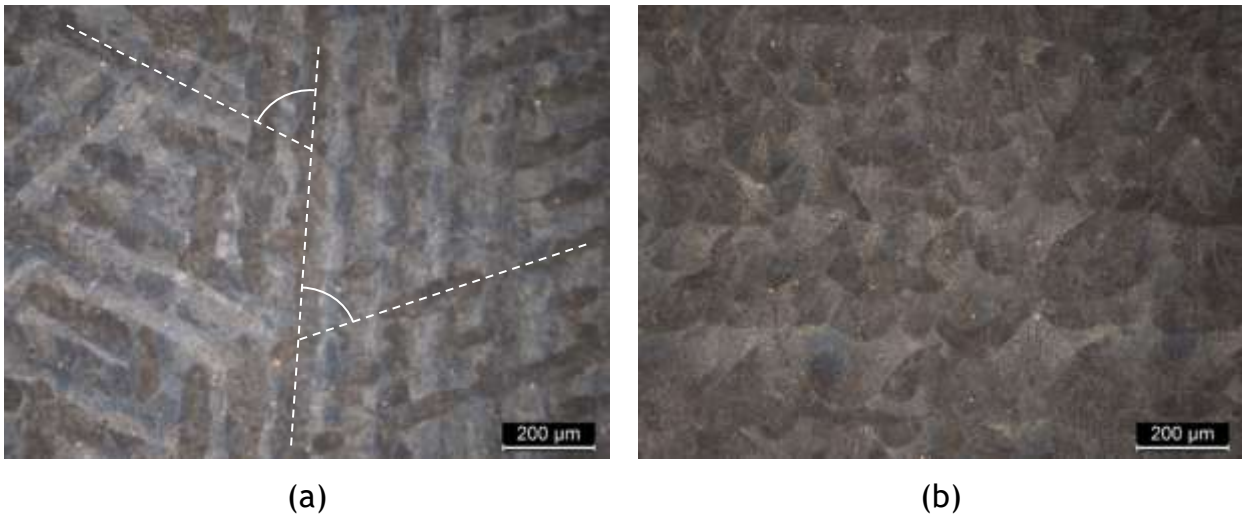

(a)   (b)

Figure 20: Top (a) and side (b) view of etched x496 sample.

4.2.3 Microstructure

Figures 21 to 23 depict the etched microstructure in side-view, revealing the expected fine columnar/cellular structure and indication of epitaxial growth (dashed red lines in figures 21 to 23), mostly at layer-layer MPB but also across track-track MPB, that in some observed cases extends vertically through the whole MP centreline across several consecutive layer-layer boundaries. Although the microstructure displays some location-specific textural orientation along the Z-axis of the sample, with mostly columnar grains at the centreline of the MP transverse cross-sections, regions closer to the lateral boundaries of the MP exhibit a highly variable texture, consisting of equiaxed cells (blue arrows in figures 21 to 23) and columnar grains (yellow arrows in figures 21 to 23), with various orientations. In general, the microstructure does not seem to have a consistent overall oriented texture. As expected, (section 2.7) from the solidification conditions, the microstructure is highly refined; cells are typically below 1 µm across.
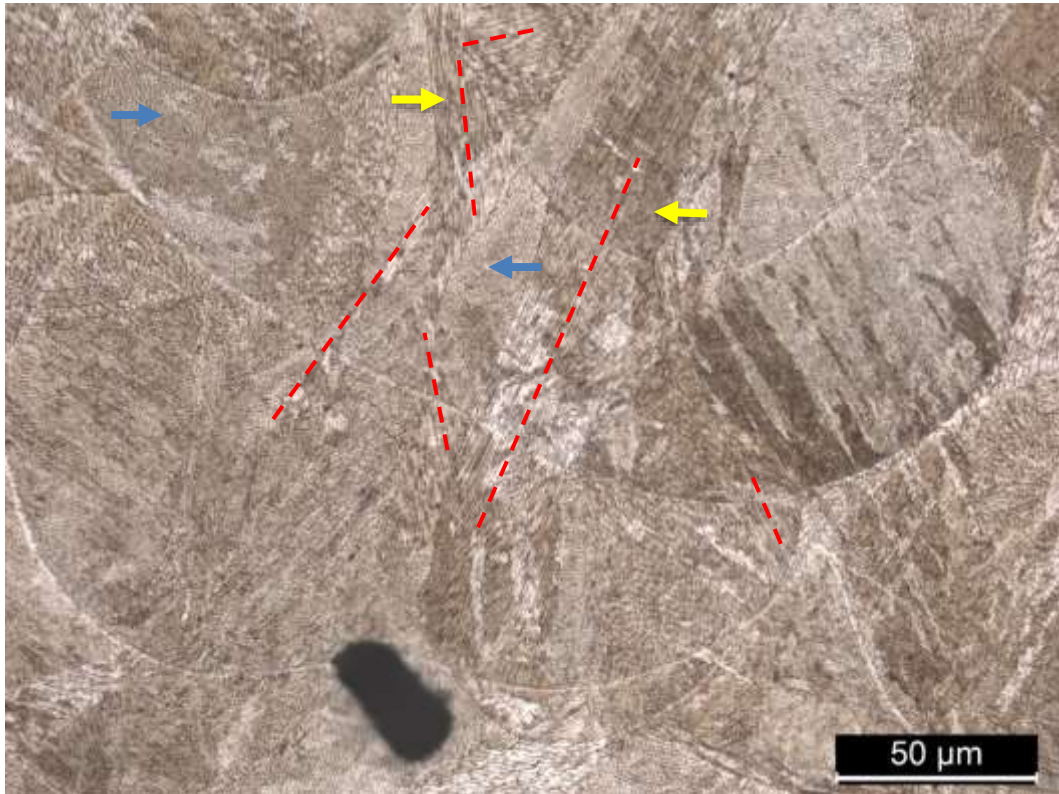
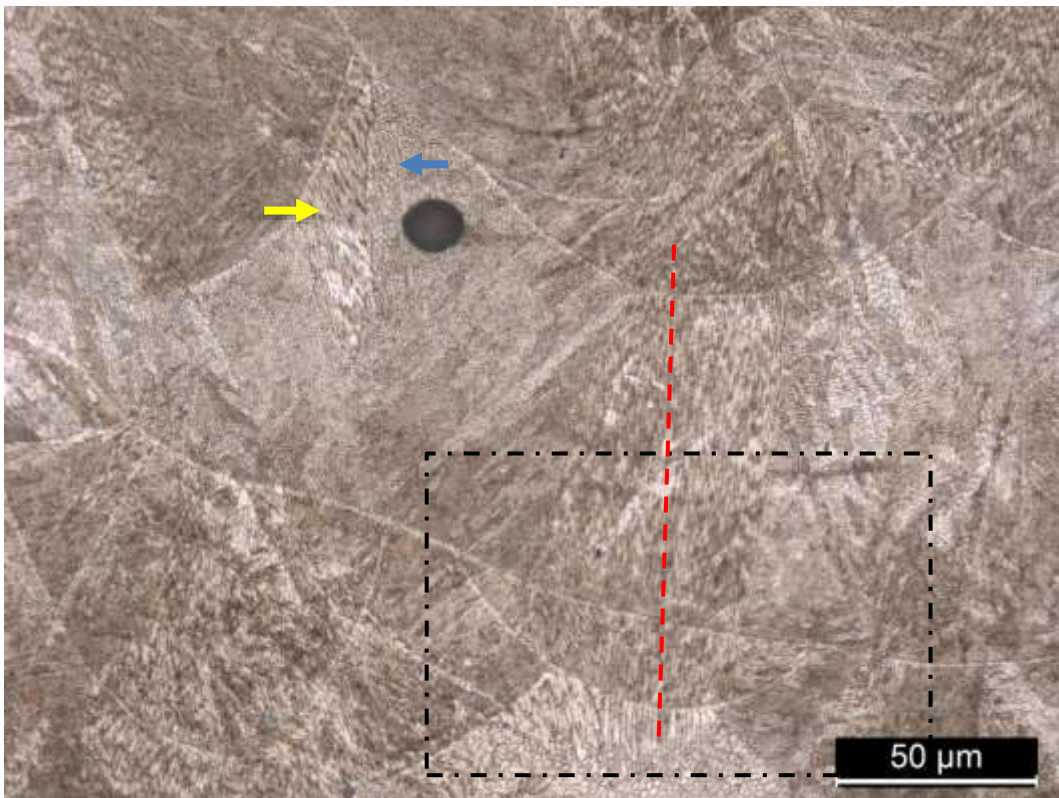Figure 21: Side-view OM image of etched sample x467.

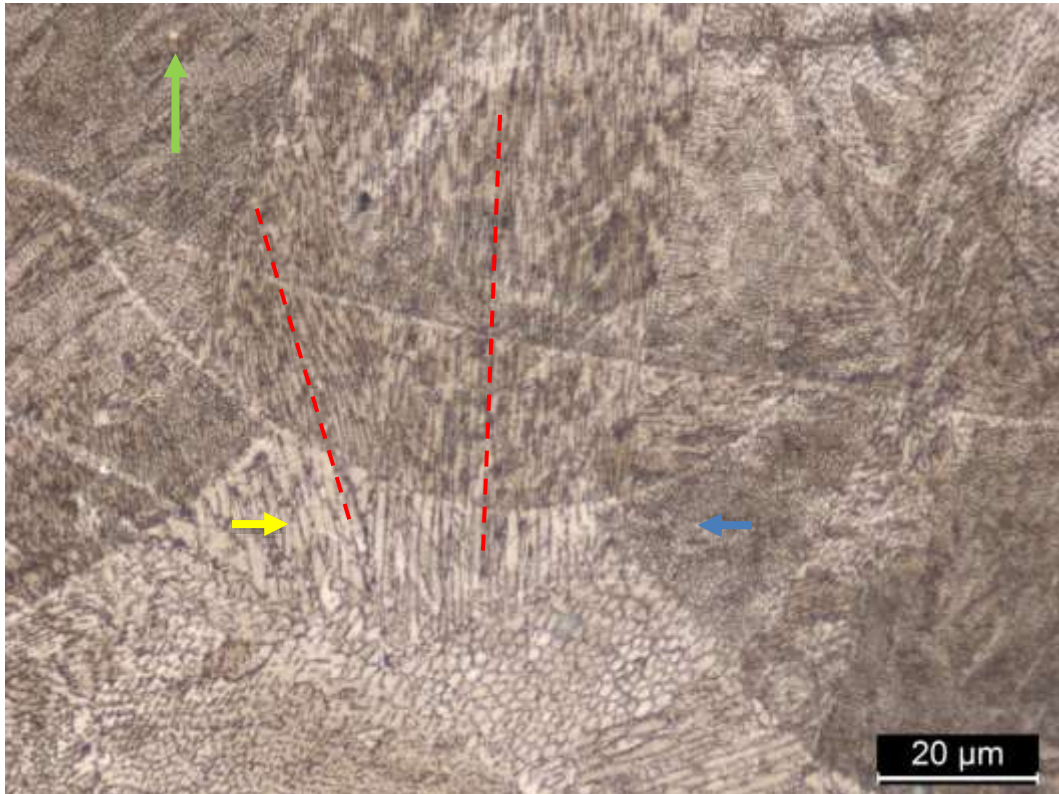Figure 22: Side-view OM image of etched sample x467.

Figure 23: Magnification of the highlighted area in Figure 22.

TiN particles, usually seen within Ti-Al oxide inclusions, were also observed in the matrix [46] (green arrow in Figure 23), which displays almost no bulk porosity, except for a few highly spherical ones, probably powder-induced (Figure 22).

4.2.4 Defects

Figure 24a shows a SEM image of samples aged at 490 °C representing the prevalent bulk structure of most observed surfaces, exhibiting a relatively homogeneous distribution of mostly equiaxed inclusions and almost no pores. Some surfaces observed presented an inconsistent distribution of inclusions, showing areas of distinguishable higher concentration of inclusions relative to most of the matrix (Figure 24b).

Inclusions may account for less than a square millimetre of the examined surface, forming patches of higher defect concentration, or they may occupy a significant area of a few square millimetres (Figure 24b). The zones of higher concentration of inclusions usually present a wide range, in size and shape, of irregular inclusions within the same area.

Very irregularly shaped inclusions always seem to have interacted with track boundaries, typically interfacing with MPB, especially highly jagged long ones and those having one or more concave boundaries, seemingly wetting MPB. Figures 25 and 26 show SEM images of highly irregular defects with remnant cracked oxides within. Figures 26a and b, present the same inclusion in OM and SEM, respectively; the former revealing a shared MPB, interfacing with the inclusion.
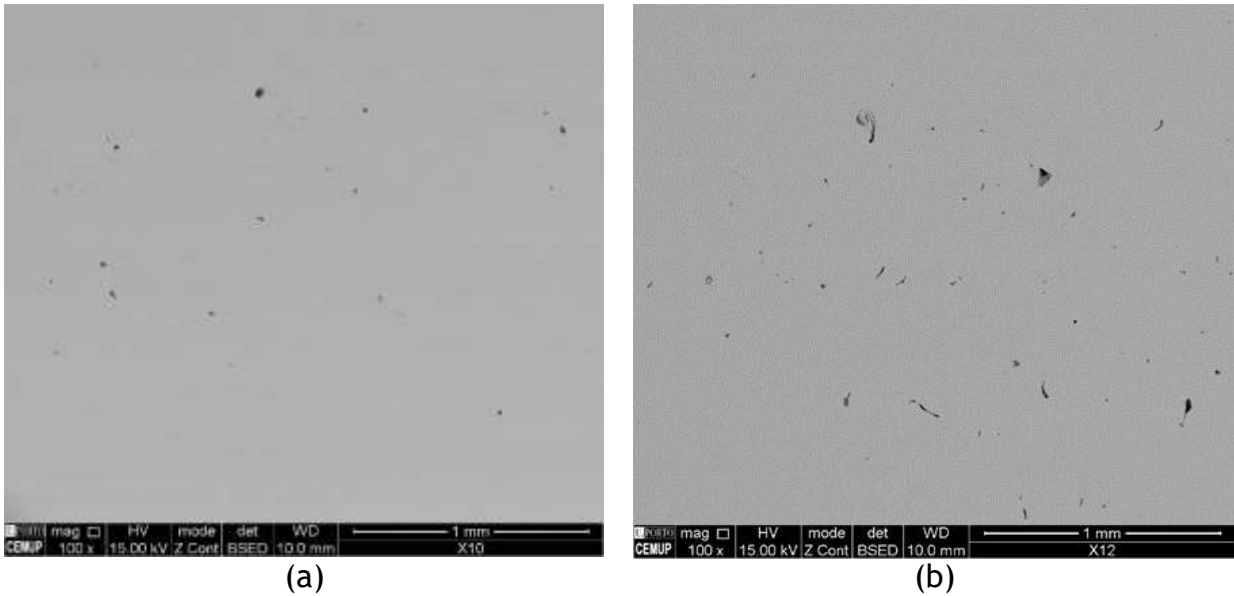

(a)   (b)

Figure 24: Top-view SEM image of samples x496 (a) and x498 (b)

(a)   (b)
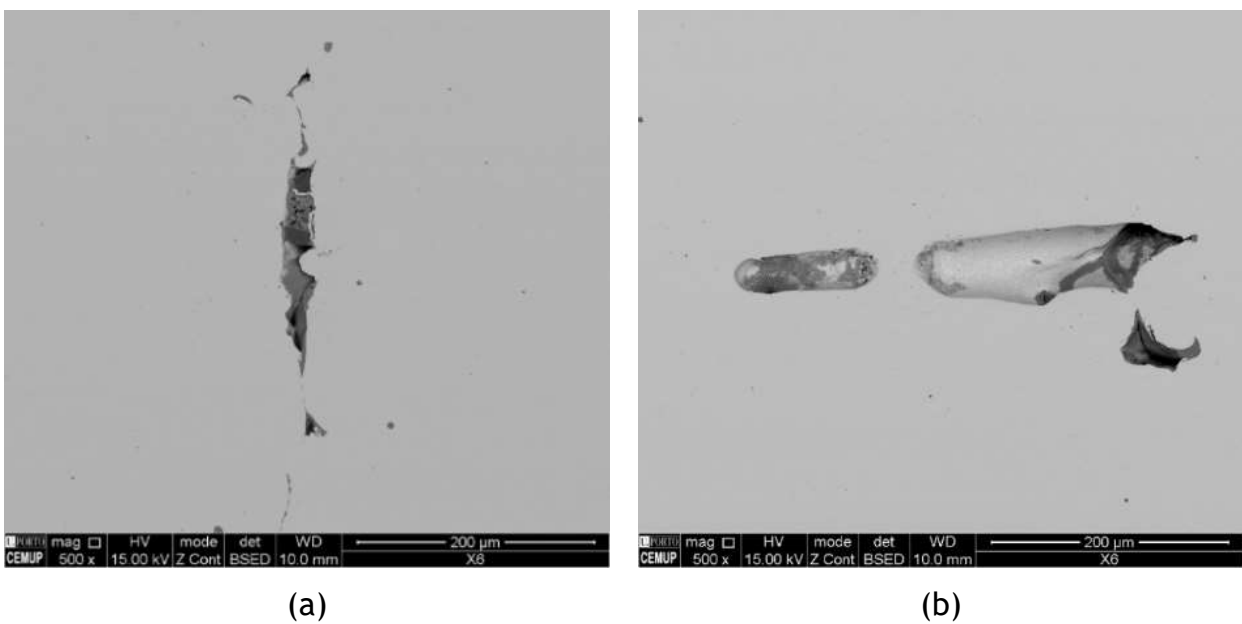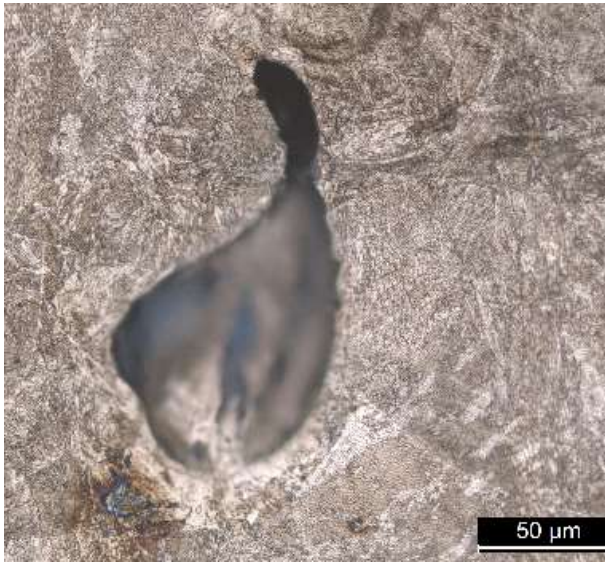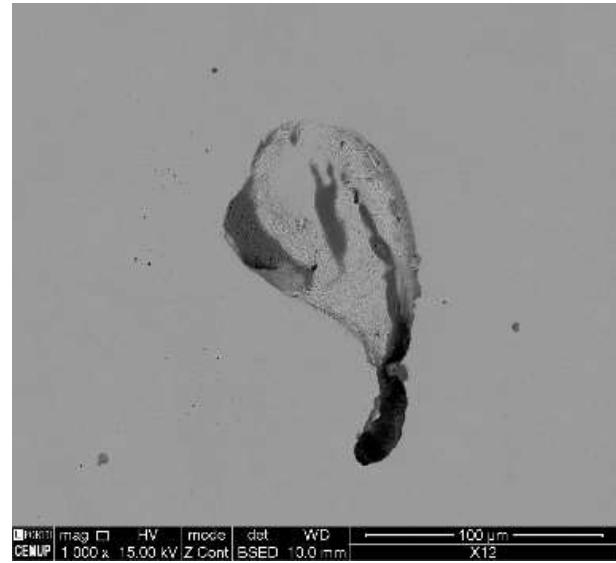
Figure 25: Side-view SEM images of defects on sample x6 (as-built)

(a)   (b)

Figure 26: OM (a) and SEM (b) images of defects on sample x498.

All irregular pores observed in the bulk matrix contained enough traces of Al-Ti oxides to suggest they were once filled with it. Although the contours are very distinct, one being very jagged (Figure 25a) and the other with aligned, smooth, cylindrical geometry (Figure 25b), both voids seem to depress deeper into the matrix suggesting connected porosity extending below. Both comprise hemispheric matrix structures, reminiscent of MPB, protruding into the inclusions, which the oxides seem to have surrounded.

Perfectly round inclusions (Figure 27) appear within the MP or diametrically intersected by MPB; these rarely exceed 25 µm across, typically below 10 µm, and are evenly distributed throughout the matrix. The spherical inclusion depicted in figure 27b contains several phases analysed via EDS and distinguishable in SEM by the different grey tone, comprising: titanium nitride, in medium grey within the inclusion (Z1 in figure 27b and respective EDS spectra in figure 28a); titanium and aluminum combined oxides, the darker grey filling most of the inclusion (Z2 in figure 27b and respective EDS spectra in figure 28b), which has been reported throughout literature [10, 11, 14]; multiple alloy particles of composition similar to the matrix, including the larger spherical centre seed particle and another irregularly shaped to its right and a myriad of other spheroid particles, well under one micron across, scattered throughout the bulk of the inclusion, some concentrically [10, 46].
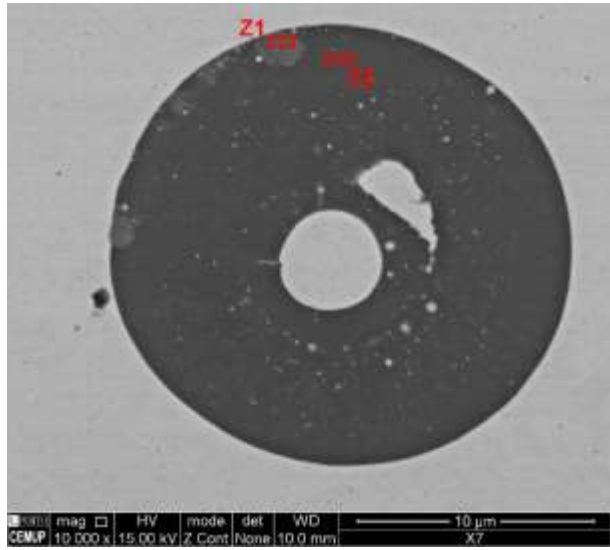
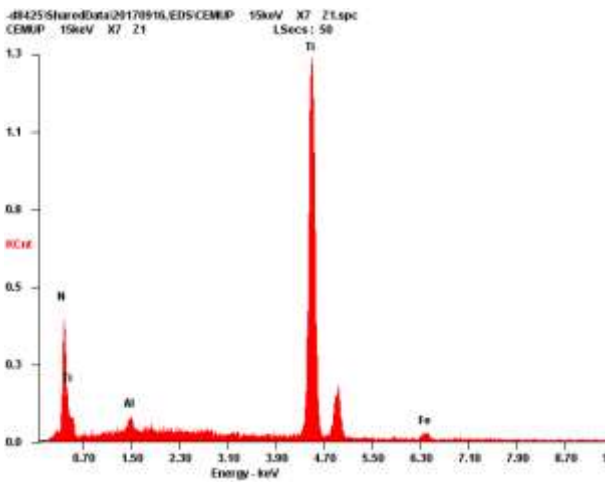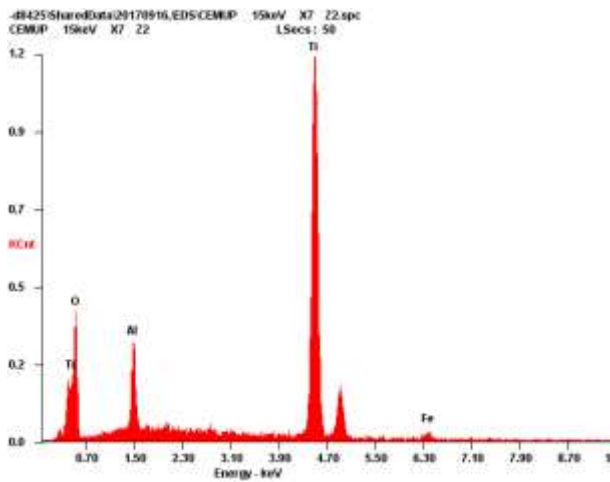(a)   (b)

Figure 27: OM (a) and SEM (b) image of spherical inclusions.

(a)   (b)

Figure 28: EDS analysis of zone 1 (a) and zone 2 (b) in figure 27b.

Several TiN particles are frequently found within inclusions of SLM-processed MS (Figure 27a); some amidst the matrix (Figure 23). These appear as 5 μm yellow squares in OM. Figure 29a shows an amplification of such phases in different growing stages within an oxide inclusion, from amorphous specs to round 1 μm particles, then to bigger polygon shaped ones and, finally, to about 5 μm cubic structures. The heterogenous nucleation of TiN particles on inclusions that are stable in liquid steel above the liquidus temperature has been evoked by several researchers [66]; the incorporation of TiN-containing oxides by the solidification front has been modelled during solidification of a MS [67].
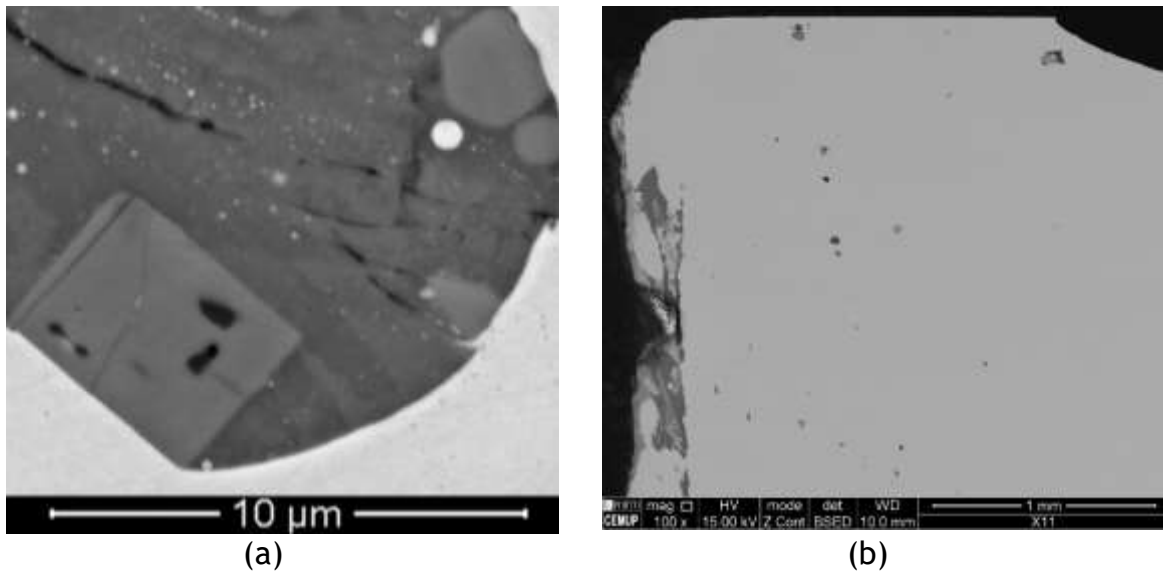
Figure 29: SEM images of TiN particles in a Ti-Al inclusion (a) and top-view of sample x497 showing an incomplete convex surface structure (left edge) with oxide-covered open porosity (b), from EDS analysis.

Figure 29b shows a cross-section top-view of sample x497. The left edge is part of a convex surface exhibiting an incomplete structure covered with cracked Ti-Al oxides. This Ti-Al oxide coating is typically found in top surfaces of SLM-processed MS, covering the side edges of scan tracks [14, 46]. Thijs *et al*. [46] studied the effect of O_2 content in the chamber atmosphere on inclusion formation during SLM of MS. The equipment's standard N_2 atmosphere (0.5 O_2 %vol) and another with a 1-2 %vol of O_2 were evaluated. They found many large and irregular inclusions (10-100 μm across) containing TiN particles and a higher concentration of inclusions at track and island borders. Under both atmospheres, an oxide layer (figure 29b), containing TiN particles, forms on top of each solidified layer. The oxide layer is mostly composed of Ti_3O_5, Al_2O_3, and Ti_2O_3 for lower O_2 %vol. The Ti/Al oxides ratio is about 85:15, consistent with their relative amount in the alloy. Both, re-melting and higher O_2 content, increase oxide thickness and spread [46].

In MS, Al and Ti have the strongest affinity to O, hence their preferential oxidation. Ti and O form different types of oxides in molten steel, such as TiO, TiO_2, Ti_2O_3 and Ti_3O_5, depending on temperature and melt and atmosphere composition [46, 68, 69]. In liquid iron, at 1873 K, Ti_2O_3 is reported to be the most stable from 0.26 to 3.6 wt%Ti, while both, Ti_2O_3 and Ti_3O_5, may coexist at around 0.25 wt%Ti; Ti_3O_5 is the most stable below 0.21 wt%Ti [68]. The high relative stability (equilibrium growth/dissolution temperatures >2000

K) of Al_2O_3 and Ti_3O_5 in liquid low alloy steels has been assessed by several researchers [69]. Extreme temperatures are localised beneath the laser spot [36]. Re-melting recovers the conditions for high Ti and Al oxides growth rate (1900-2000 K) [69], since most of the surface liquid in the transition and tail sections of the MP (in quasi-steady-state) is below 2100 K [36]. The high atmospheric N_2 content is likely to promote TiN growth, which growth rate is higher than that of oxides at lower temperatures (~1700K) [69].

The scanning of each layer partially re-melts the previously consolidated one, during which the cracked oxide layer is fragmented by the laser. The fragmented oxides are either captured by the fast solidifying MP, or they float to its top due to their lower density and MP flow, in which case they are dragged by the surface tension driven flow (Marangoni effect), thereby accumulating at the track boarders where temperatures are lower, thus more suited to oxide growth [69]. The floating oxides can also be dragged by the laser along its path and accumulate at the end of scan vectors or laser manoeuvres [46].

(a)   (b)
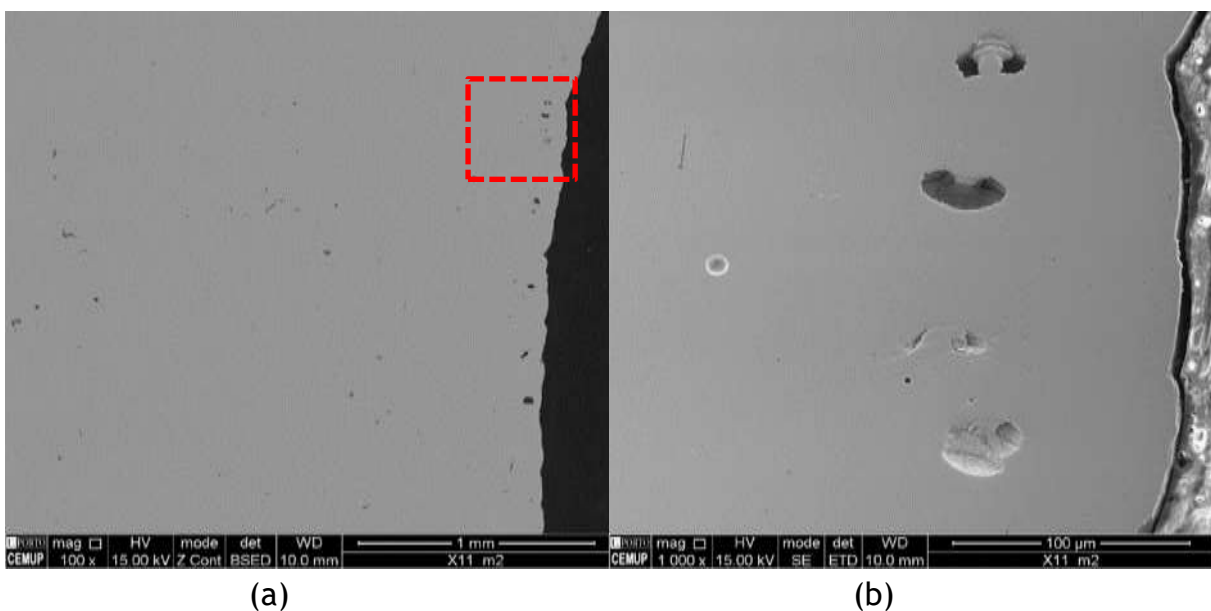
Figure 30: (a) SEM image of an edge of sample x497 and (b) a magnification of the highlighted area in (a).

Figure 30 presents side-views of sample x467 showing surface-aligned porosity; this was observed in all samples from batch 1. Figure 31 shows similar defects and surrounding microstructure. Copious observations were made of globular pores near the bottom of tracks (Figure 31a) parallel to vertical or curved surfaces, around 100 µm along the normal to that surface (Figure 31b); most often without oxide traces within these pores.

(a)   (b)

Figure 31: Metallographic side (a) and top (b) view of recurring edge pores.

Although *sky-witting* (Figure 9b) entails a sudden laser shut down (section 2.4.3.2), pores at the end of scan vectors (Figure 7b) were rarely seen. OM observations showed no evidence of a proper peripherical contour pass (section 2.5.2); moreove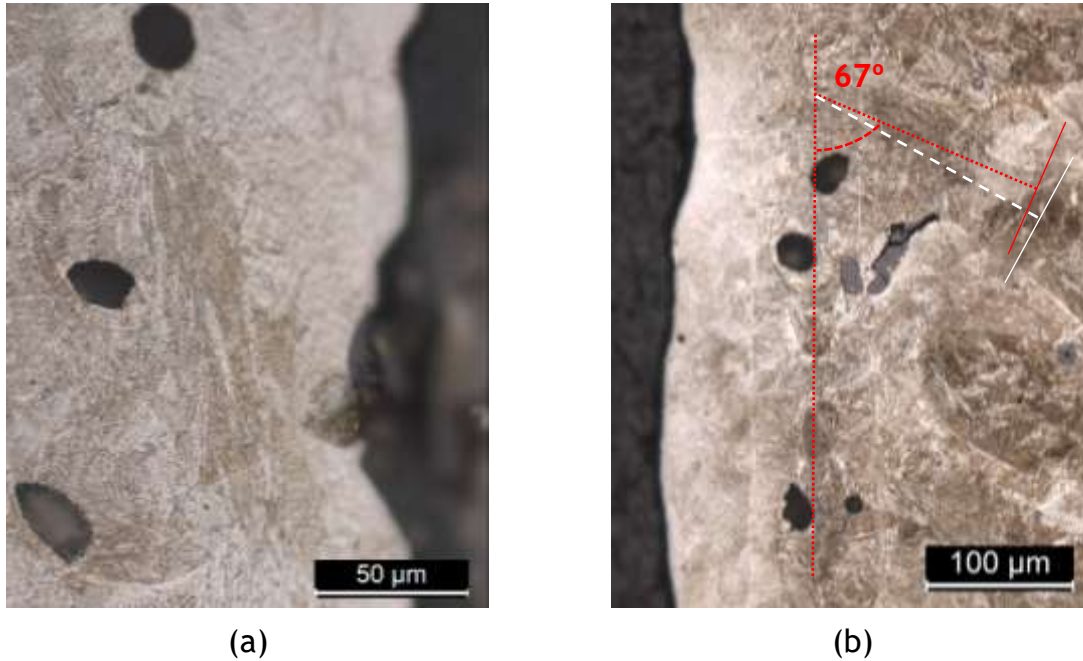r, cross-section views of vertically consecutive MP (figure 31a) are not wide enough (considering spot size), nor do they change width between them significantly, as to be considered tracks with different orientations, so they are probably parallel to the surface. The DMLS scanning pattern starts with the layer contour. The diameter of the melted zone is larger than that of the laser spot, so it is shifted inwards by half its diameter, this is the beam offset [44]. When tracks parallel to the edges were observed in top-view (Figure 31b), their centreline is typically about 100 μm from the edge, twice the allegedly normal beam offset. Moreover, no tracks parallel to those were observed further into the bulk structure, nor were they at 67º to other tracks. Vectors along the edges are more prone to overheating (section 2.5.3), hence to high heat-input induced-porosity (section 2.6.1). The end of scan vectors is also prone to overheating (section 2.5.3), particularly with bi-directional raster scanning (section 2.5.2) since the laser quickly returns to partially re-melt that vector's end, and to oxide accumulation, whereby oxides are dragged by the laser path flow, thereby seeding defects and affecting the wetting conditions for the formation of subsequent overlying tracks (section 2.4.3.2 and 2.6.1) [36, 41].

5 Conclusions

The components used to test aging heat treatment conditions presented huge differences in surface roughness between top, bottom and vertical surfaces. Top surfaces were the smoothest despite the hilly topology. Vertical surfaces had a highly layered relief of varying magnitude along the same surface. Bottom (overhanging) surfaces also presented high roughness, reminiscent of its interaction with the underlying loose powder. Transition surfaces were also very irregular; incomplete in some cases.

The microstructure, despite exhibiting the expected features of SLM-processed Maraging steels, varied considerably in terms of defect concentration. Some cross-sections showed a high concentration of large irregular inclusions while other exhibited very few; also, the distribution of defects within each surface can varied significantly. Ti-Al oxide inclusions probably result from an excess of oxygen dissolved in the melt, which promotes the formation of an oxide layer over the recently consolidated surfaces that is subsequently broken and is either captured by the fast solidifying melt pool or float to its top.

Despite no appreciable porosity being found, only a few round pores likely from gas entrapment, all samples showed large (~50 µm) pores consistently about 100 µm from the surface.

The highest hardness values were obtained with a 6-hour holding stage at 490 ℃, therefore, these were the aging conditions applied to the tensile test specimens.

The tensile test samples also displayed considerable differences in surface roughness depending on the surface orientation, although generally lower and more consistent along each surface.

Aged tensile test samples yielded mechanical performance similar to the highest reported in literature for Maraging C-300 steel produced by SLM, i.e., high yield strength (~1950 MPa) and ultimate tensile strength (~2000 MPa), very low ductility (~2%). and particularly high Young's modulus (~250 GPa) The specimens did not display appreciable anisotropy. The as-built tensile performance was also comparable to literature reported values and the samples built horizontally provided slightly better results.

References

[1] I. Gibson, D. W. Rosen, B. Stucker, *Additive manufacturing technologies: Rapid Prototyping to Direct Digital Manufacturing,* 2010, New York, NY, Springer.

[2] NIST, *Measurement Science Roadmap for Metal-Based Additive Manufacturing*, US Department of Commerce, National Institute of Standards and Technology, Prepared by Energetics Incorporated, May 2013.

[3] W.E. Frazier, *Direct Digital Manufacturing of Metallic Components: Vision and Roadmap*, Solid Free Form Fabrication Proceedings, University of Texas at Austin, Austin TX, (2010) 717–732.

[4] W. Frazier, *Metal additive manufacturing: a review*, J. Mater. Eng. Performance, 23 (2014) 1917–1928.

[5] ASTM-International, standard terminology for additive manufacturing technologies, F2792-12a, 2013.

[6] ASM International Handbook Committee, *ASM Handbook, Volume 01-Properties and Selection: Properties and Selection: Irons, Steels, and High-Performance Alloys*, 10th ed.,1990, ASM International.

[7] ASM International Handbook Committee, *ASM Handbook, Volume 4-Heat Treating*, 10th ed., 1991, ASM International.

[8] W. Sha, *Steels: From Materials Science to Structural Engineering*, Springer, 2013.

[9] W.J. Sames, F.A. List, S. Pannala, R.R. Dehoffn, S.S. Babu, *The metallurgy and processing science of metal additive manufacturing*, International Materials Reviews, 2016.

[10] E. Yasa, K. Kempen, J. Kruth, *Microstructure and mechanical properties of maraging steel 300 after selective laser melting*, Proceedings of the 21st Annual International Solid Freeform Fabrication Symposium, Austin, TX, 2010, 383-396.

[11] K. Kempen, E. Yasa, L. Thijs, J. Kruth, J. van Humbeeck, *Microstructure and mechanical properties of Selective Laser Melted 18Ni-300 steel*. Phys. Proc., 12 (2011) 255–263.

[12] G. Casalino, S.L. Campanelli, N. Contuzzi, A.D. Ludovico, *Experimental investigation and statistical optimisation of the selective laser melting process of a maraging steel*, Optics and Laser Technology, 65 (2015) 151-158.

[13] H. B. Thorsten, D Dimitrov, *The achievable mechanical properties of SLM produced Maraging Steel 300 components*, Rapid Prototyping Journal, 22(3) (2016) 487-494.

[14] C.L. Tan, K.S. Zhou, X. Tong, Y.S. Huang, J. Li, W.Y. Ma, F.H. Li, T.C. Kuang, *Microstructure and mechanical properties of 18Ni-300 maraging steel fabricated by selective laser melting*, Proceedings of the 2016 6th International Conference on Advanced Design and Manufacturing Engineering, 96 (2016) 404–410.

[15] R. Casati, J.N. Lemke, A. Tuissi, M. Vedani, *Aging behaviour and mechanical performance of 18-Ni 300 steel processed by selective laser melting*, Metals, 6(9) (2016) 218.

[16] H. Gu, H. Gong, D. Pal, K. Rafi, T. Starr, B. Stucker, *Influences of energy density on porosity and microstructure of selective laser melted 17-4PH stainless steel*, Solid freeform fabrication symposium, Austin, TX, 2013.

[17] EOS-MS1-Maraging Steel Material data sheet,
https://cdn.eos.info/1deee2b550955632/b3615b80c80a/MS-MS1-M290_Material_data_sheet_10-17_en.pdf
https://cdn0.scrvt.com/eos/c88047245bff2c4b/2f494ef432d0/MS-MS1-M280_M290_400W_Material_data_sheet_05-14_en.pdf

[18] ASTM-International, *Standard test methods for flow rate of metal powders using the Hall Flowmeter funnel*, B213-13, ed. West Conshohocken, PA, ASTM International, 2013.

[19] ASTM-International, *Standard test method for apparent density of free-flowing metal powders using the Hall Flowmeter funnel*, B212-13, ed. West Conshohocken, PA, ASTM International, 2013.

[20] A. Santomaso, P. Lazzaro, P. Canu, *Powder flowability and density ratios: the impact of granules packing*, Chem. Eng. Sci., 58 (2003) 2857–2874.

[21] D. D. Gu, W. Meiners, K. Wissenbach, R. Poprawe, *Laser additive manufacturing of metallic components: materials, processes and mechanisms*, Int. Mater. Rev., 57 (2012) 133–164.

[22] W. J. Sames, F. Medina, W. H. Peter, S. S. Babu, R. R. Dehoff, *Effect of process control and powder quality on Inconel 718 produced using electron beam melting*, Superalloy 718 and derivatives, Pittsburgh, PA, 2014.

[23] B. Liu, R. Wildman, C. Tuck, I. Ashcroft, R. Hague: *Investigation the effect of particle size distribution on processing parameters optimization in selective laser melting process*, Solid Freeform Fabrication Symposium, Austin, TX, 2011, 60.

[24] A. B. Spierings, N. Herres, G. Levy. *Influence of the particle size distribution on surface quality and mechanical properties in AM steel parts*. Rapid Prototyping Journal, 17 (3) (2011) 195–202.

[25] N.K. Tolochko, S.E. Mozzharov, I.A. Yadroitsev, T. Laoui, L. Froyen, V.I. Titov, M.B. Ignatiev. *Balling processes during selective laser treatment of powders*. Rapid Prototyping J, 10 (2004) 78–87.

[26] D.D. Gu, Y.F. Shen. *Balling phenomena in direct laser sintering of stainless-steel powder: metallurgical mechanisms and control methods*, Materials and Design, 30(8) (2009) 2903–10.

[27] C. Qiu, C. Panwisawas, M. Ward, H. Basoalto, J Brooks, M. Attallah, *On the role of melt flow into the surface structure and porosity development during selective laser melting*, Acta Materialia, 96 (2015) 72–9.

[28] S. Rahmati, E. Vahabli, *Evaluation of analytical modeling for improvement of surface roughness of FDM test part using measurement results*. Int J Adv Manuf. Technol., 79(5–8) (2015) 823–9.

[29] H. Lee, C.H.J. Lim, M.J. Low, N. Tham, V.M. Murukeshan, Y-J. Kim, *Lasers in additive manufacturing: A review*. Int. J. Precis. Eng. Manuf. Green Technol., 4 (2017) 307–322.

[30] S. Li, G. Chen, S. Katayama, Y. Zhang, *Relationship between spatter formation and dynamic molten pool during high-power deep-penetration laser welding*, Appl. Surf. Sci., 303 (2014) 481–488.

[31] A.V. Gusarov, J.-P. Kruth, *Modelling of radiation transfer in metallic powders at laser treatment*, International Journal of Heat and Mass Transfer, 48 (2005) 3423–3434

[32] C. D. Boley, S. C. Mitchell, A. M. Rubenchik, S. S. Q Wu, *Metal powder absorptivity: modeling and experiment*, Appl. Opt., 55 (2016) 6496–6500.

[33] N.K. Tolochko, Y.V. Khlopkov, S.E. Mozzharov, M.B. Ignatiev, T. Laoui, V.I. Titov, *Absorptance of powder materials suitable for laser sintering*, Rapid Prototyping Journal, 6(3) (2000).155-161.

[34] D. Bergström, J. Powell, A.F.H. Kaplan, *The absorptance of steels to Nd:YLF and Nd:YAG laser light at room temperature*, Applied Surface Science, 253, (2007), 5017–5028.

[35] I. Yadroitsev, I. Yadroitsava, *Evaluation of residual stress in stainless steel 316L and Ti6Al4V samples produced by selective laser melting*, Virtual and Physical Prototyping, 10(2) (2015) 67-76.

[36] S.A. Khairallah, A.T. Anderson, A. Rubenchik, W.E. King, *Laser powder-bed fusion additive manufacturing: physics of complex melt flow and formation mechanisms of pores, spatter, and denudation zones*, Acta Materialia., 108 (2016) 36-45.

[37] T. DebRoy, H.L. Wei, J.S. Zuback, T. Mukherjee, J.W. Elmer, J.O. Milewski, A.M. Beese, A. Wilson-Heid, A. Ded, W. Zhang, *Additive manufacturing of metallic components – Process, structure and properties*, Progress in Materials Science, 92 (2018) 112–224.

[38] S.I. Anisimov, V.A. Khokhlov, *Instabilities in Laser-matter Interaction*, CRC, Boca Raton, Fl, 1995.

[39] Tien T. Roehling, Sheldon S.Q. Wu, Saad A. Khairallah, John D. Roehling, S. Stefan Soezeri, Michael F. Crumb, Manyalibo J. Matthews, *Modulating laser intensity profile ellipticity for microstructural control during metal additive manufacturing*, Acta Materialia, 128 (2017) 197-206.

[40] L. N. Carter, M. M. Attallah and R. C. Reed, *Laser powder bed fabrication of nickel-base superalloys: influence of parameters; characterisation, quantification and mitigation of cracking*, Superalloys 2012: 12th International Symposium on Superalloys, (ed. E.S. Huron *et al.*), 2012, 577–586, Champion, PA, John Wiley & Sons, Inc.

[41] L. Thijs, F. Verhaeghe, T. Craeghs, J. V. Humbeeck, J-P Kruth, *A study of the microstructural evolution during selective laser melting of Ti-6Al-4V*, Acta Mater., 58 (2010) 3303-3312.

[42] H. Gong, K. Rafi, H. Gu, G.D.J. Ram, T. Starr, B. Stucker, *Influence of defects on mechanical properties of Ti-6Al-4V components produced by selective laser melting and electron beam melting*, Materials & Design, 86 (2015) 545-554.

[43] W. E. King, H. D. Barth, V. M. Castillo, G. F. Gallegos, J. W. Gibbs, D. E. Hahn, C. Kamath, A. M. Rubenchik, *Observation of keyhole-mode laser melting in laser powder-bed fusion additive manufacturing*, J. Mater. Process. Technol., 214 (2014) 2915–2925.

[44] D. Manfredi, F. Calignano, M. Krishnan, R. Canali, E. Ambrosio, S. Biamino, D. Ugues, M. Pavese, P. Fino, *Additive Manufacturing of Al Alloys and Aluminium Matrix Composites (AMCs)*, Ch. 1, InTech, (http://creativecommons.org/licenses/by/3.0), 2014, DOI: 10.5772/58534.

[45] J. Suryawanshi, K.G. Prashanth, U. Ramamurty, *Tensile, fracture, and fatigue crack growth properties of a 3D printed maraging steel through selective laser melting*, Journal of Alloys and Compounds, 725 (2017) 355-364.

[46] L. Thijs, J. Van Humbeeck, K. Kempen, E. Yasa, J. Kruth, M. Rombouts, *Investigation on the inclusions in maraging steel produced by Selective Laser Melting*, Innovative Developments in Virtual and Physical Prototyping: Proceedings of the 5th International Conference on Advanced Research in Virtual and Rapid Prototyping, Leiria, Portugal, September, CRC Press, 2011, 297.

[47] S. Das, *Physical Aspects of Process Control in Selective Laser Sintering of Metals*, Adv. Eng. Mater., 5 (2003) 701–711.

[48] J.P. Kruth, L. Froyen, J.Van Vaerenbergh, P. Mercelis, M. Rombouts, B. Lauwers. *Selective laser melting of iron-based powder*, J. Mater. Process. Technol., 149 (2004) 616–622.

[49] A. Gusarov, I. Smurov, *Modeling the interaction of laser radiation with powder bed at selective laser melting*, Phys. Proc., 5 (2010) 381–94.

[50] R. Li, J. Liu, Y. Shi, L. Wang, and W. Jiang, *Balling behaviour of stainless steel and nickel powder during selective laser melting process*, Int. J. Adv. Manuf. Technol., 59 (2011) 1025–1035.

[51] P. Mercelis, J.P. Kruth, *Residual stresses in selective laser sintering and selective laser melting*, Rapid Prototyping Journal, 12(5) (2006) 254–265.

[52] T.Gnäupel-Herold, J. Slotwinski and S.Moylan, *Neutron measurements of stresses in a test artifact produced by laser-based additive manufacturing*, AIP Conference Proc., 1581 (2014) 1205–1212.

[53] L. M. Sochalski-Kolbus, E. A. Payzant, P. A. Cornwell, T. R. Watkins, S. S. Babu, R. R. Dehoff, M. Lorenz, O. Ovchinnikova, C. Duty, *Comparison of Residual Stresses in Inconel 718 Simple Parts Made by Electron Beam Melting and Direct Laser Metal Sintering*, Metall. Mater. Trans. A, 46 (2015) 1419–1432.

[54] A. S. Wu, D.W. Brown, M. Kumar, G. F. Gallegos and W. E. King, *An experimental investigation into additive manufacturing induced residual stresses in 316L stainless steel*, Metall. Mater. Trans. A, 45 (2014) 6260–6270.

[55] K. Kempen, L. Thijs, B. Vrancken, S. Buls, J. Van Humbeeck, J.-P. Kruth, *Producing, crack-free, high density M2 HSS parts by selective laser melting: pre-heating the baseplate*, Solid freeform fabrication symposium, Austin, TX, 2013.

[56] M. Shiomi, K. Osakada, K. Nakamura, T. Yamashita, and F. Abe, *Residual Stress within Metallic Model Made by Selective Laser Melting Process*, CIRP Ann., 53 (2004) 195–198.

[57] W. Kurz, B. Giovanola, R. Trivedi, Theory of microstructural development during rapid solidification. Acta Metall., 34(5) (1986) 823–30.

[58] J.J. Blecher, T.A. Palmer, T. DebRoy, *Solidification map of a nickel-base alloy. Metall*, Mater Trans A, 45A (4) (2014) 2142–51.

[59] M. Garibaldi, I. Ashcroft, M. Simonelli, R. Hague, *Metallurgy of high-silicon steel parts produced using Selective Laser Melting*. Acta Mater., 110 (2016) 207–16.

[60] S.F. Wen, S. Li, Q. S. Wei, Z. Y. Yan, Z. Sheng, Y. S. Shi, *Effect of molten pool boundaries on the mechanical properties of selective laser melting parts*, J. Mater. Process. Technol., 214 (11) (2014) 2660-2667.

[61] E.A. Jägle, P.P. Choi, J. van Humbeeck, D. Raabe, *Precipitation and austenite reversion behavior of a maraging steel produced by selective laser melting*. J. Mater. Res., 29 (2014) 2072–2079.

[62] B. Song, X. Zhao, S. Li, C. Han, Q. Wei, S. Wen, J. Liu, Y. Shi, *Differences in microstructure and properties between selective laser melting and traditional manufacturing for fabrication of metal parts: A review*, Front. Mech. Eng., 10(2) (2015) 111–125.

[63] J. Lewandowski, M. Seifi, *Metal Additive Manufacturing: A Review of Mechanical Properties*, Annu. Rev. Mater. Res., 46 (2016) 151–86.

[64] L. Hitzler, J. Hirsch, B. Heine, M. Merkel, W. Hall, A. Öchsner, *On the Anisotropic Mechanical Properties of Selective Laser-Melted Stainless Steel*, Materials, 10 (2017) 1136.

[65] M.V. Diamanti, S. Codeluppi, A. Cordioli, M.P. Pedeferri, *Effect of thermal oxidation on titanium oxides' characteristics*, J. of Experimental Nanoscience, 4(4) (2009) 365-372.

[66] V. Descotes, J-P. Bellot, V. Perrin-Guérin, S. Witzke, A. Jardy, *Titanium nitride (TiN) precipitation in a maraging steel during the vacuum arc remelting (VAR) process - Inclusions characterization and modeling*, Int. Symp. on Liquid Metal Processing & Casting 2015, IOP Conf. Ser.: Materials Science and Engineering, 143(1) (2016) 012013.

[67] V. Descotes, J-P. Bellot, S. Witzke, A. Jardy, *Modeling the titanium nitride (TiN) germination and growth during the solidification of maraging steel*, Int. Symp. on Liquid Metal Processing & Casting, (2013) 201–206.

[68] J-J. Pak, J-O. Jo, S-I. Kim, W-Y. Kim, T-I. Chung, S-M. Seo, J-H Park, D-S Kim, *Thermodynamics of Titanium and Oxygen Dissolved in Liquid Iron Equilibrated with Titanium Oxides*, ISIJ International, 47(1) (2007) 16–24.

[69] T. Hong, T. DebRoy, *Effects of time, temperature, and steel composition on growth and dissolution of inclusions in liquid steels*, Ironmaking and Steelmaking, 28(6) (2001) 450-454.